HHS Public Access

Author manuscript

Nat Struct Mol Biol. Author manuscript; available in PMC 2024 February 01.

Published in final edited form as:

Nat Struct Mol Biol. 2023 September ; 30(9): 1365–1379. doi:10.1038/s41594-023-01010-x.

Microtubule binding-induced allostery triggers LIS1 dissociation from dynein prior to cargo transport

William D. Ton[1,†], **Yue Wang**[2,†], **Pengxin Chai**[2,†], **Cisloynny Beauchamp-Perez**[1], **Nicholas T. Flint**[1], **Lindsay G. Lammers**[1], **Hao Xiong**[2], **Kai Zhang**[2,‡], **Steven M. Markus**[1,‡]

[1]Department of Biochemistry and Molecular Biology, Colorado State University, Fort Collins, Colorado, USA

[2]Department of Molecular Biophysics and Biochemistry, Yale University, New Haven, Connecticut, USA

Abstract

The lissencephaly-related protein LIS1 is a critical regulator of cytoplasmic dynein that governs motor function and intracellular localization (*e.g.,* to microtubule plus-ends). Although LIS1 binding is required for dynein activity, its unbinding prior to initiation of cargo transport is equally important, since preventing dissociation leads to dynein dysfunction. To understand whether and how dynein-LIS1 binding is modulated, we engineered dynein mutants locked in a microtubule-bound (MT-B) or -unbound (MT-U) state. Whereas the MT-B mutant exhibits low LIS1 affinity, the MT-U mutant binds LIS1 with high affinity, and as a consequence remains almost irreversibly associated with microtubule plus-ends. We find that a monomeric motor domain is sufficient to exhibit these opposing LIS1 affinities, and that this is evolutionarily conserved between yeast and humans. Three cryo-EM structures of human dynein with and without LIS1 reveal microtubule-binding induced conformational changes responsible for this regulation. Our work reveals key biochemical and structural insight into LIS1-mediated dynein activation.

INTRODUCTION

Cytoplasmic dynein-1 is a highly conserved molecular motor that transports cargos toward the minus ends of microtubules. The dynein complex is comprised of several accessory chains and two copies of the ~500 kDa heavy chain, the latter of which possesses all of the elements required for motility[1]. Processive motility requires that dynein first be released from an autoinhibited state referred to as the 'phi' particle[2–4], and that it then associate with

Contact information for corresponding authors: Steven M. Markus, steven.markus@colostate.edu, Kai Zhang, jack.zhang@yale.edu.
†These authors contributed equally
‡These authors jointly supervised this work

AUTHOR CONTRIBUTIONS

S.M.M. designed the study. W.D.T., C.B.-P., N.T.F., L.G.L., and S.M.M. purified yeast proteins, whereas W.D.T., C.B.-P., and S.M.M. purified human proteins. L.G.L. performed ATPase assays with MT-U and MT-B proteins. W.D.T., N.T.F, and S.M.M. performed *in vitro* binding assays. W.D.T., N.T.F., L.G.L., and S.M.M. performed and analyzed live-cell microscopy. Y.W. and P.C. acquired and analyzed cryo-EM data, and built PDB models with support from K.Z. H.X. and Y.C. performed molecular dynamics simulations. S.M.M., Y.W., P.C., L.G.L. and S.M.M. generated figures. S.M.M. wrote the manuscript. W.D.T, Y.C., P.C., K.Z., and S.M.M. edited and revised the manuscript. S.M.M. and K.Z. acquired funding.

COMPETING INTERESTS

The authors declare no competing interests.

its activating complex dynactin, and a cargo adaptor that links dynein to dynactin and a variety of cargoes[5,6].

A critical regulator of dynein is the lissencephaly-related protein LIS1 (also known as Platelet-Activating Factor Acetylhydrolase IB subunit Beta, or PAFAH1B1), mutations in which lead to dynein dysfunction and severe neurodevelopmental disorders[7,8]. Recent studies support a model whereby LIS1 binding to dynein prevents it from adopting the phi conformation[2,7,9–11]. LIS1 has also been shown to promote dynein's association with microtubule plus ends[12–17], and to aid in the recruitment of a second dynein complex to dynactin, thereby stimulating formation of faster motor complexes[10,11,18,19].

Although LIS1 binding to dynein is required for it to promote these activities, it is less clear whether LIS1 remains bound to dynein during cargo transport. Single molecule motility assays have revealed varying extents of comigration of LIS1 with dynein. Whereas one study noted robust colocalization of LIS1 with motile dynein-dynactin-adaptor (DDA) complexes (~75%)[18], others have noted much lesser extents of binding (from ~15% to ~30%[2,10,11]), in spite of the large excess of LIS1 used in all these assays. Reconstitution of DDA behavior on dynamic microtubules revealed that LIS1 associates with and promotes plus end binding of dynein (via EB1), but appears to dissociate prior to initiation of motility, since only a small fraction of minus end-directed DDA complexes possessed detectable LIS1[20]. This latter finding is consistent with data from budding yeast in which overexpression of the dynein-dynactin-binding domain of the cargo adaptor Num1 appears to promote assembly and motility of DDA complexes that do not colocalize with Pac1, the yeast homolog of LIS1[21]. Moreover, LIS1 homologs in filamentous fungi were found to only transiently associate with retrograde-moving dynein-driven endosomes[22,23]. Finally, although Pac1 associates with dynein at the plus ends of microtubules in budding yeast, it does not colocalize with dynein at its site of activity in this organism: the cell cortex[12,24]. Together, these data favor a model in which LIS1 and its homologs likely dissociate from dynein prior to initiation of cargo transport.

Whether dissociation of dynein from LIS1 is required for cargo transport in metazoa is unclear. However, one piece of evidence from budding yeast suggests that their dissociation is indeed crucial. Specifically, inclusion of bimolecular fluorescence complementation (BiFC) tags on Pac1 and Dyn1 (the latter of which encodes the dynein heavy chain) leads to a situation in which these two proteins remain associated subsequent to delivery of dynein-dynactin to cortical Num1 (due to the irreversible association of the two split-YFP halves)[25,26]. Whereas those cells expressing only one of the two BiFC-tagged proteins possess normal dynein function, those expressing both exhibit defects in dynein function as severe as those lacking Dyn1, suggesting that dynein-Pac1 dissociation is critical for proper in-cell dynein activity.

Our understanding of LIS1 and Pac1 function is complicated by conflicting findings regarding these molecules' abilities to modulate dynein's microtubule-binding activity, thereby affecting its velocity, and its ability to remain associated with microtubule plus ends[27–29]. Arguments against this model include findings that a Pac1-bound dynein does not employ its microtubule-binding domain (MTBD) to associate with plus ends in cells[21],

and that the extent of Pac1's ability to reduce dynein velocity *in vitro* scales with Pac1's microtubule-binding[2,7]. Since Pac1 does not bind microtubules in cells[12,25], these findings force us to reevaluate whether Pac1 and LIS1 actually impact dynein mechanochemistry. Determining whether LIS1 remains associated with motile dynein-dynactin complexes in cells will help to clarify these controversies.

Here we set out to address the question of whether and how dynein-LIS1 affinity is modulated, and to determine whether microtubule binding by dynein may be responsible. We engineered dynein mutants constitutively locked in either a microtubule-unbound or -bound conformational state. Our data reveal that these mutants indeed reflect the native conformations of dynein in these two states, and that they have opposing affinities for LIS1. Specifically, the microtubule-unbound state of dynein exhibits higher affinity for LIS1 than the microtubule-bound state. We find that the motor domain of dynein is sufficient for this behavior, and that it is conserved from yeast to humans. Cells expressing the microtubule-unbound dynein mutant exhibit robust dynein-Pac1 binding, but little unbinding, and exhibit behavior consistent with an inability of dynein to dissociate from the plus end-binding machinery, and thus the plus ends themselves. Our observations indicate that dynein must switch to a microtubule-bound conformation in order to dissociate from LIS1, which then permits the adoption of a motility-competent state of the DDA complex. High-resolution cryo-electron microscopy (cryo-EM) structures reveal the structural basis for microtubule-binding-induced dissociation of dynein-LIS1. Our data are consistent with a model in which LIS1 must dissociate from dynein prior to initiation of cargo transport, and that microtubule-binding is responsible for triggering this dissociation.

RESULTS

Generation of microtubule-unbound and -bound dynein mutants

We previously found that binding of the yeast cargo adaptor protein Num1 to dynein-dynactin triggers dissociation of Pac1 from dynein, thus promoting minus end-directed motility of the motor complex[21]. However, deletion of dynein's MTBD prevented this dissociation, suggesting that dynein must bind microtubules for this to occur. We thus sought to determine whether microtubule-binding triggers dissociation of dynein from Pac1. Microtubule binding by dynein leads to a conformational change in the MTBD that is communicated to the AAA+ ring via a translation of the CC1 helix of the dynein stalk with respect to CC2, causing a change in the heptad registry of this coiled-coil (Extended Data Fig. 1A)[30–33]. We hypothesized that this helix shift initiates events that leads to dynein-Pac1 dissociation.

To test this, we used a previously employed protein engineering strategy in which the dynein MTBD and short regions of CC1 and CC2 are replaced with a stable coiled-coil derived from seryl tRNA synthetase (SRS_{CC})[34]. By including or excluding 4 amino acids in CC1, sufficient to encode a single turn in this helix (Extended Data Fig. 1B), we aimed to lock CC1 in either an up or down state, thus reflecting the microtubule-bound or -unbound state, respectively[33]. Consistent with previous work using *Dictyostelium discoideum* dynein[34], the microtubule-unbound (MT-U) and -bound (MT-B) mutants exhibit ATPase rates that closely match that of wild-type dynein in the absence and presence of microtubules,

respectively (Extended Data Fig. 1C). As expected, neither mutant possesses microtubule-binding activity (Extended Data Fig. 1D).

Dynein mutants exhibit opposing localization behaviors

The extent to which dynein and Pac1 interact governs the degree to which these proteins localize to various sites in cells (*e.g.*, microtubule plus ends). For example, cells with no Pac1 exhibit an almost complete lack of dynein foci[12,17], while those overexpressing Pac1 or expressing a dynein mutant with higher-than-wild-type affinity for Pac1 both exhibit a greater number of dynein foci[2,24,25]. Thus, the number and brightness of dynein foci directly correlate with dynein-Pac1 affinity. Imaging cells expressing Pac1–3mCherry and either dynein$^{MT\text{-}U}$-3YFP or dynein$^{MT\text{-}B}$-3YFP revealed that these two mutants exhibit opposing degrees of dynein localization. Specifically, dynein$^{MT\text{-}U}$-expressing cells exhibit more plus end and cortical foci than wild-type cells, while only a small fraction of dynein$^{MT\text{-}B}$-expressing cells exhibit foci. Moreover, intensity measurements revealed that dynein$^{MT\text{-}U}$ foci were much brighter than dynein$^{MT\text{-}B}$ (Fig. 1A–C, non-hatched bars).

The pattern of Pac1 localization in these cells reflects that of the respective dyneins (Fig. 1A–C, hatched bars). Whereas neither wild-type nor *dyn1$^{MT\text{-}B}$* cells possess Pac1 foci at the cell cortex, a large fraction of *dyn1$^{MT\text{-}U}$* cells do, almost all of which colocalize with dynein$^{MT\text{-}U}$ (Fig. 1A and C). Given that Pac1 is never observed at the cortex in wild-type cells, we wondered whether Bik1 (homolog of human CLIP-170) also localizes to cortical sites in *dyn1$^{MT\text{-}U}$* cells. Bik1 is required for plus end association of dynein and Pac1, and makes a tripartite complex with these proteins at plus ends[17,24,25]. Imaging *dyn1$^{MT\text{-}U}$* cells expressing Bik1–3mCherry revealed that this protein also ectopically localizes to cortical sites (Fig. 1D). Whereas some cortical Bik1 foci were not associated with microtubules (magenta arrowheads and bars in Fig. 1D and E), others were simultaneously associated with the cortex and a microtubule plus end (red arrowheads and bars). Time-lapse imaging revealed that plus ends remain anchored at cortical sites in *dyn1$^{MT\text{-}U}$* cells for much longer than in wild-type or *dyn1$^{MT\text{-}B}$* cells, with some lasting throughout the entire 30-minute imaging period (Fig. 1F–H, and Video S1). We confirmed the plus ends were anchored via canonical cortical dynein complexes by deleting Num1, which resulted in a large reduction in these events (Fig. 1G and H).

These data indicate that dynein is in a microtubule-unbound conformation at plus ends, and that it must switch to a microtubule-bound state to dissociate from Pac1. Failure to do so results in dynein remaining bound to Pac1 and the microtubule plus end via Bik1.

Allostery within dynein motor domain governs Pac1 affinity

To determine the minimal region of dynein that is sufficient to exhibit differential Pac1 affinity, we assessed the localization of a motor domain truncation (Fig. 2A). This region (dynein$_{MOTOR}$), which encompasses the AAA+ ring and most of the linker element is sufficient for Pac1 binding and thus for localizing to plus ends[35]. This fragment is missing a region of the linker that was previously found to encounter Pac1 during its powerstroke (arrow, Fig. 2A)[27]. Whereas dynein$_{MOTOR}$$^{MT\text{-}U}$-3YFP exhibits a similar extent of plus end binding as wild-type dynein$_{MOTOR}$, dynein$_{MOTOR}$$^{MT\text{-}B}$-3YFP was present in fewer cells, and

with a lower fluorescence intensity (Fig. 2B and C). Thus, the structural determinants that account for differential Pac1 affinity are contained within the motor domain.

To determine whether dynein and Pac1 are sufficient to exhibit this behavior *in vitro*, we combined purified dynein$_{MOTOR}$ and Pac1, and applied them to a size exclusion chromatography column. Pac1 comigrated with dynein$_{MOTOR}^{MT\text{-}U}$ to a greater extent than dynein$_{MOTOR}^{MT\text{-}B}$, indicating that Pac1 binds dynein$_{MOTOR}^{MT\text{-}U}$ with greater affinity than dynein$_{MOTOR}^{MT\text{-}B}$ (Fig. 2D).

To validate these findings, we employed mass photometry, a microscopy-based single molecule method that permits determination of the masses of protein species within a mixture[36]. Analysis of each protein alone revealed that the large majority of each had mass values consistent with dimeric Pac1, and monomers of each dynein (Fig. 3A and Extended Data Fig. 2A). We then mixed Pac1 with each dynein$_{MOTOR}$ fragment and assessed the proportion of species that resulted. In the presence of ATP, we noted a ~two-fold greater proportion of dynein$_{MOTOR}^{MT\text{-}U}$-Pac1 complexes (see ~520 kDa peak) than dynein$_{MOTOR}^{MT\text{-}B}$-Pac1 complexes (Fig. 3B–D). This was also true across a range of Pac1 concentrations (Extended Data Fig. 2B). This also revealed that wild-type dynein$_{MOTOR}$ bound to Pac1 with an affinity that was almost identical to dynein$_{MOTOR}^{MT\text{-}U}$ (Fig. 3D and Extended Data Fig. 2A), which is consistent with the notion that this mutant mimics wild-type microtubule-unbound dynein.

The nucleotide-bound state of dynein affects Pac1 affinity

Previous studies found that dynein-LIS1 binding is enhanced by treatment with ATP and vanadate[29], which results in an ADP-Pi-like state[37]. To determine how different nucleotides affect the ability of MT-U or MT-B to bind Pac1, we repeated our mass photometry experiments with either no nucleotide (“apo”), AMPPNP (non-hydrolyzable ATP), ATP and vanadate (Vi), or ADP. As expected, ADP-Vi indeed enhances Pac1 binding for both wild-type dynein$_{MOTOR}$ and dynein$_{MOTOR}^{MT\text{-}U}$ (Fig. 3B–D and Extended Data Fig. 2A); however, Pac1-dynein$_{MOTOR}^{MT\text{-}B}$ binding is unaffected by ADP-Vi. AMPPNP also strongly enhances Pac1 binding to dynein$_{MOTOR}$ and dynein$_{MOTOR}^{MT\text{-}U}$, but only has a minor effect on dynein$_{MOTOR}^{MT\text{-}B}$. Interestingly, apo conditions led to a situation in which all three dynein$_{MOTOR}$ fragments bound to Pac1 with similar affinities. Finally, ADP had a minor enhancing effect for Pac1 binding to all three fragments. Given the similar response of dynein$_{MOTOR}$ and dynein$_{MOTOR}^{MT\text{-}U}$ in all conditions, these data further support the notion that these two fragments are structurally and biochemically similar, whereas the dynein$_{MOTOR}^{MT\text{-}B}$ mutant is distinct, and may represent the bona fide microtubule-bound state of dynein (see Supplementary Results).

In light of the inability of ADP-Vi to affect the Pac1-binding affinity of dynein$_{MOTOR}^{MT\text{-}B}$, we wondered whether this mutant can bind Vi. To address this, we mixed the dynein$_{MOTOR}$ fragments with ATP in the absence or presence of Vi, and exposed them to ultraviolet light. Although wild-type and dynein$_{MOTOR}^{MT\text{-}U}$ underwent Vi-dependent photocleavage indicative of Vi binding to AAA1, dynein$_{MOTOR}^{MT\text{-}B}$ did not, indicating that the microtubule-bound conformation has a low affinity for Vi (and by extension, Pi; Extended

Data Fig. 3). Thus, treatment with ATP and Vi does not enhance the Pac1-binding affinity of dynein$_{MOTOR}^{MT-B}$ because it is unable to bind Vi (see Supplementary Discussion).

Allostery governing LIS1 affinity is conserved in humans

To determine whether the phenomenon we have described thus far is conserved with human proteins, we purified LIS1 and corresponding human dynein$_{MOTOR}$ fragments from insect cells, and assessed their binding via mass photometry. This revealed a very similar difference in LIS1-binding affinity between the two mutants in ATP (Fig. 4B–D). Repeating the binding experiments in the presence or absence of different nucleotides revealed an almost identical response of the human proteins to LIS1 binding as the yeast proteins (Fig. 4D and Extended Data Fig. 2C). The only notable differences between the yeast and human proteins were a somewhat stronger enhancement of LIS1 binding for both mutants by the apo state, and a more pronounced stimulation by ADP. These data indicate that microtubule-binding induced conformational changes also reduce the affinity of human dynein for LIS1.

Cryo-EM structures of human MT-B and LIS1-bound MT-U dynein

Our data thus far indicate that dynein$_{MOTOR}^{MT-U}$ behaves almost identically to wild-type dynein with respect to LIS1-binding, but that dynein$_{MOTOR}^{MT-B}$ exists in a low LIS1-affinity state. To determine the structural basis for this behavior, we obtained 3.4 and 3.2 Å cryo-EM structures for human dynein$_{MOTOR}^{MT-B}$ alone and a LIS1-bound dynein$_{MOTOR}^{MT-U}$, respectively (Fig. 5A, Extended Data Fig. 4A–J, and Table 1). While dynein$_{MOTOR}^{MT-B}$ was frozen in the presence of ATP, we froze dynein$_{MOTOR}^{MT-U}$ in the presence of ATP and Vi to enrich for LIS1-bound complexes. We were able to unambiguously assign nucleotide densities to all 4 binding pockets in both dyneins (Extended Data Fig. 5A and E). Although ADP-Vi was apparent in AAA1 of dynein$_{MOTOR}^{MT-U}$, the AAA1 pocket of dynein$_{MOTOR}^{MT-B}$ was bound to ADP, suggesting that the microtubule-bound state of dynein has a high affinity for ADP at AAA1. This is consistent with a recent report in which ADP was observed at AAA1 for a native microtubule-bound dynein-dynactin-adaptor complex[38].

Comparisons to published structures revealed varying degrees of similarities (Figs. 5B and C, Extended Data Fig. 5B, C and G, and Table S1). Notably, that which most closely resembles dynein$_{MOTOR}^{MT-B}$ is the native microtubule-bound dynein described above. The minor differences between these two structures can be accounted for by the presence of AMPPNP instead of ADP at AAA3 in the native microtubule-bound dynein (Extended Data Fig. 5D). Consistent with our data indicating that dynein$_{MOTOR}^{MT-U}$ behaves like wild-type dynein in the absence of microtubules, its structure very closely resembles that of the ADP-Vi-bound dynein-2 (Fig. 5C and Table S1). These data indicate that our mutants indeed reflect microtubule-unbound and -bound conformations, and that the latter is distinct from that adopted by a microtubule-unbound dynein in the presence or absence of various nucleotide analogs.

Our dynein$_{MOTOR}^{MT-U}$-LIS1 structure revealed the monomeric motor bound to two LIS1 WD40 beta-propellers (Fig. 5A). Given our mass photometry data indicate a 1:1 binding stoichiometry (1 LIS1 dimer:1 dynein motor), these two beta-propellers are likely from the

same LIS1 homodimer (Extended Data Fig. 6A and C). Consistent with previous structures of yeast dynein bound to a Pac1 dimer[39,40], the LIS1 beta-propellers were bound to two sites on the human dynein motor: one at the interface of AAA3 and AAA4 (referred to as site^{ring}), and the other at the base of the stalk (site^{stalk}). Binding of LIS1 to site^{ring} involves a surface exposed helix in AAA4, a short loop within AAA5, and part of a longer loop within AAA3, while binding at site^{stalk} involves residues along the stalk, part of a long loop within AAA4, and residues at the tip of the buttress (Fig. 5D, Extended Data Figs. 6B and 7, and Video S2). We also noted contacts between the two LIS1 beta-propellers. All of these contacts are consistent with those identified in a recent structure of a yeast dynein-Pac1 complex[39], and also with a very recent structure of wild-type human dynein bound to LIS1[41] (Extended Data Fig. 6B, Fig. S1, and Table S1), further supporting the notion that dynein$^{MT\text{-}U}$ reflects the native microtubule-unbound dynein.

Inspection of the LIS1 regions that contact site^{ring} and site^{stalk} revealed numerous residues distributed over the face of the two beta-propellers (Extended Data Figs. 6B and 8, and Video S2). Although one of these residues (H277) has been found to be mutated in a patient with lissencephaly[42], four others have been found to be mutated in cancer patients (Fig. 5E and F; M172T, R238H, D338G, and F382L)[43]. We used molecular dynamics (MD) simulations to analyze the potential consequences of these mutations on the dynein-LIS1 interaction, and found that the cancer-correlated mutations all decrease the energy of interaction to varying degrees, while the lissencephaly-correlated mutation did not (Fig. 5G and Extended Data Fig. 6D). These data suggest that weakened LIS1-dynein interactions caused by M172T, R238H, D338G, or F382L may be linked to tumorigenesis.

An analysis of our dynein$_{MOTOR}^{MT\text{-}U}$-LIS1 cryo-EM dataset revealed that a subset of these dyneins were bound to only 1 LIS1 (36%), while the remaining were either bound to 2 (29%) or “1.5” molecules (34%), in which a strong density was apparent for only one of the LIS1 molecules, with a weaker density corresponding to the 2nd LIS1, which is indicative of flexibility of this latter molecule (Extended Data Fig. 4F). All LIS1-bound dyneins possess clear density at site^{ring}, indicating this is the primary binding site, while the presence of the site^{stalk}-bound LIS1 was variable, suggesting that this site is the lower affinity LIS1-binding site on dynein. Local resolution analysis of the three classes revealed that the density for the site^{ring}-bound LIS1 is best for the 1.5 and 2 LIS1-bound dyneins (as determined by the resolution of the bound LIS1; Extended Data Fig. 9A). Moreover, all three classes exhibit clear density for ADP within the AAA3 binding pocket, suggesting that the nucleotide state is not causative of these differences (Extended Data Fig. 9B). These observations suggest that the binding of LIS1 to site^{stalk}, which appears to be rate-limiting, stabilizes the entire LIS1 dimer-dynein complex. In addition to the improved resolution of LIS1, we also noted that two regions at site^{stalk} also exhibit greater resolution when more than 1 LIS1 is present: the AAA4 loop (residues 3111–3138), and the tip of the buttress, suggesting these regions become less flexible when bound to LIS1 (Extended Data Fig. 9B).

Cryo-EM structure of human MT-U dynein without LIS1

The reduced flexibility of the LIS1-binding regions of dynein, as well as previously published work suggest that LIS1 binding may affect the conformation of dynein[28,40].

It remains controversial whether this binding affects dynein's mechanochemistry and/or microtubule-binding behavior[7]. We reasoned that if LIS1 were to impact the biochemical behavior of dynein, its binding would cause structural changes reflective of these activities. To determine if this is the case, we solved a 2.9 Å cryo-EM structure of dynein$_{MOTOR}^{MT-U}$ in the absence of LIS1, but in the presence of ATP and Vi (to allow an accurate comparison with the LIS1-bound dynein). With a few exceptions, this revealed a structure that was almost identical to the LIS1-bound dynein$_{MOTOR}^{MT-U}$ (Fig. 6A and B). Notably, the conformation of the nucleotide binding pocket at AAA3, which was clearly bound to ADP, appears unchanged between the LIS1-bound and unbound dynein (Fig. 6C). Among the exceptions are the following small differences at the LIS1-binding sites (Fig. 6D): the tip of the buttress is shifted 3.1 Å toward the site^{stalk}-bound LIS1, which results in a 1.7 Å shift of CC2 toward CC1 of the stalk; and, the AAA5 loop is shifted 1.4 Å away from the site^{ring}-bound LIS1. The overall conformational similarities between these two dynein structures are consistent with recent findings that LIS1 does not in fact impact dynein's mechanochemistry or microtubule-binding behavior[2]. Rather, our findings suggest that dynein's conformational state impacts its ability to bind LIS1, but not vice versa.

The linker domain is thought to adopt one of two states: a pre-powerstroke state, in which the linker is bent by ~90°, and a post-powerstroke state, in which the linker is straight[44–46]. Given that ATP and vanadate promotes the adoption of the pre-powerstroke state[37] and stimulates dynein-LIS1 binding[29], it is possible that a straight linker precludes LIS1 binding due to the close proximity of LIS1 to the N-terminus of the linker, and thus potential steric hinderance[27]. Although our dynein^{MT-B} structure clearly possesses a straight linker (Fig. 5A), the N-terminal region of the linker of both LIS1-bound and -unbound dynein^{MT-U} exhibited significant flexibility of this region, in spite of the presence of ATP and vanadate. Using 3D classification, we found that this region samples a range of conformations, from bent to straight (Extended Data Fig. 10). These observations suggest that the linker conformation is not necessarily predictive of LIS1-binding.

Changes at the ring site account for reduced LIS1 affinity

Global alignment of MT-U and MT-B reveal the changes initiated by microtubule binding and the consequent CC1/CC2 helix sliding in the stalk[47]. Movement of CC2 with respect to CC1 causes the tip of the buttress to shift away from the AAA+ ring. This leads to a deep kink in the middle of the buttress, and a consequent rigid body movement of the AAA5S-AAA6L subdomains. This causes the AAA+ ring to adopt a more open state that can no longer coordinate Pi binding at AAA1 (Extended Data Fig. 5H and Video S3). We wondered whether these changes spanning one side of the AAA+ ring (AAA1, AAA5, AAA6) lead to allostery on the other side (*i.e.*, at site^{ring} and site^{stalk}) that would influence dynein-LIS1 affinity. Local alignment of MT-U and MT-B using AAA4-AAA5 revealed several notable changes at both LIS1 binding interfaces, including the following: at site^{stalk}, the tip of the buttress is shifted 10.3 Å away from LIS1 (Fig. 7A); at site^{ring}, both the AAA4 helix (residues 2886–2903) and the AAA3 loop (residues 2875–2880) are shifted 4.4–6.5 Å away from the AAA5 loop (residues 3654–3661), thus increasing the spacing between these three elements that all make direct contacts with LIS1 (Figs. 5D and 7B; also see Video

S4). This latter change is likely sufficient to significantly weaken LIS1's binding affinity for site^{ring}.

Our data suggest that LIS1-binding to dynein is initiated at site^{ring}, and followed by site^{stalk}. This is further supported by the fact that a monomeric Pac1 binds predominantly at site^{ring} with no apparent binding at site^{stalk27}. Thus, we sought to determine if structural changes at site^{ring} are responsible for the altered Pac1 and LIS1-binding affinity. To this end, we specifically interrogated this site by assessing the binding between dynein and a monomeric Pac1 mutant (lacking its N-terminal dimerization domain; Pac1$^{\Delta N}$). We found that, much like the Pac1 dimer, Pac1$^{\Delta N}$ binds dynein$_{MOTOR}{}^{MT\text{-}U}$ to a significantly greater extent than dynein$_{MOTOR}{}^{MT\text{-}B}$ (Fig. 7C). To ensure that Pac1$^{\Delta N}$ was binding to site^{ring} we repeated this binding assay using dynein variants with three point mutations that interfere with Pac1-site^{stalk} binding: E3012A, Q3014A, and N3018A ("EQN" mutant)[40]. This revealed an identical binding disparity of Pac1$^{\Delta N}$ for the MT-U and MT-B mutants (Fig. 7C, bottom). We validated these findings in cells by assessing the localization of EQN dynein$_{MOTOR}{}^{MT\text{-}U}$ and dynein$_{MOTOR}{}^{MT\text{-}B}$ mutants to microtubule plus ends. Although both exhibited reduced plus end localization with respect to the wild-type versions of each, the two proteins exhibited localization disparities similar to that of the wild-type MT-U and MT-B fragments (Fig. 7D and E). These data are consistent with a role for site^{stalk} in dynein-Pac1 binding, and indicate that site^{ring} indeed undergoes a conformational change that weakens its affinity for Pac1/LIS1 upon microtubule binding.

We next focused on the structural elements at site^{ring} that may account for the microtubule-binding induced Pac1/LIS1-dissociation: the AAA4 helix, the AAA3 loop, and the AAA5 loop, which move with respect to each other upon microtubule-binding (Fig. 7A and B, and Video S4). Consistent with the importance of the AAA4 helix in dynein-Pac1 binding, mutating either four residues (K2721A, D2725G, E2726S, and E2727G; "KDEE" mutant[28]) or only one (E2726A; equivalent to E2903 in human dynein) severely reduces plus end binding of both dynein$_{MOTOR}{}^{MT\text{-}U}$ and dynein$_{MOTOR}{}^{MT\text{-}B}$ in cells (Fig. 7F). Furthermore, deleting two key residues in the AAA5 loop[39] (N3475 and R3476) significantly reduces plus end binding by MT-U and MT-B (Fig. 7F), consistent with the importance of this surface in Pac1-binding[39]. We next focused on the AAA3 loop as a potential Pac1/LIS1-binding surface that changes in response to microtubule-binding. In support of the importance of this interface, which includes a salt bridge between LIS1 D388 and dynein K2879, MD simulation data reveal that the cancer-correlated D338G mutation in LIS1 significantly reduces binding energy (Fig. 5E–G and Extended Data Fig. 6D). Additional MD simulations reveal that deleting this loop (Δ2875–2880) or mutating K2879 to an alanine in human dynein, or deleting this loop in yeast dynein (Δ2678–2703) reduces binding energy between dynein and LIS1/Pac1 (Fig. 7G). Yeast cells expressing dynein$_{MOTOR}{}^{MT\text{-}U}$-3YFP and dynein$_{MOTOR}{}^{MT\text{-}B}$-3YFP mutants with this loop deleted (Δ2698–2703) exhibit significant reductions in the intensities of foci (Fig. 7F). Finally, mass photometric analysis revealed that deletion of the AAA3 loop severely reduces binding of Pac1 to dynein$_{MOTOR}{}^{MT\text{-}U}$ in spite of the presence of AMPPNP or ATP and Vi (Fig. 7H). These data demonstrate the importance of this loop in the dynein-LIS1/Pac1 contact, and indicate that the conformational changes at site^{ring} that result from microtubule binding likely account for disruption of the dynein-LIS1 complex.

DISCUSSION

Our work reveals insight into the final step of the LIS1-mediated dynein activation pathway. Our findings strongly suggest that microtubule binding by dynein triggers its dissociation from LIS1, and that this is required to uncouple the dynein transport complex from the plus end-targeting machinery (*e.g.*, Bik1/CLIP-170 in yeast, and EB1 in metazoa)[17,18,20,48]. This dissociation is required for dynein to switch from a plus end-bound state, in which it is only indirectly associated with the microtubule, to a motile state, in which it is directly engaged with the microtubule lattice. Dynein is in a microtubule-unbound conformation when it is at the plus end. Preventing its switching to a microtubule-bound state locks dynein in this plus end-associated state in cells. In light of the similar affinity of wild-type and dynein$^{MT\text{-}U}$ for Pac1/LIS1 *in vitro*, it is the microtubule-bound state that is a unique conformational state that exhibits low affinity for Pac1/LIS1. In addition to revealing the structural basis for the weakened affinity, we find that LIS1 binding to dynein is governed by the conformational state of dynein, but that LIS1 binding has no significant effect on dynein's conformation, at least in the context of our ADP-Vi-bound MT-U mutant.

We posit the following model for Pac1 function in budding yeast (see Video S5): (1) dynein stochastically switches between phi and open states in the cytoplasm[2,3]; (2) once in an open state, Pac1 binds to dynein due to the increased accessibility of Pac1-binding surfaces, thus preventing dynein from switching back to the phi particle[2,10]; (3) dynein-Pac1 binds to plus end-bound Bik1[21]; (4) dynactin associates with plus end-bound dynein; (5) dynein-dynactin binds to cortical Num1, which triggers dynein-microtubule binding, potentially by arranging the motor domains in a parallel configuration[3]; (6) microtubule-binding by dynein triggers conformational changes that include a distortion of site^{ring} that weakens its affinity for Pac1; (7) Pac1 dissociates from dynein, thus breaking dynein's indirect connection to the plus end; (8) dynein-dynactin directly engage with the microtubule, and translocate the mitotic spindle. In light of the similarities between the yeast and metazoan systems[7], and our data with human dynein and LIS1, we posit that a very similar mechanism is at play in animal cells.

Given that dynein is in a microtubule-unbound conformation at plus ends, and that the dynein MTBD is dispensable for this association[21], our work indicates that Pac1 (and likely LIS1) does not in fact promote plus end binding by impacting dynein's microtubule-binding behavior. In fact, we show that once dynein makes direct contact with the microtubule, this leads to a consequent dissociation of dynein from Pac1. This likely explains the lack of Pac1/LIS1-dynein colocalization at sites of dynein activity[22–24]. These data are further supported by our cryo-EM structures for dynein$^{MT\text{-}U}$ in the absence and presence of LIS1, which show very little differences between them.

Our work also reveals a high resolution structure of a human dynein-LIS1 complex that highlights precise residues that link these molecules together. Our 3D classification analysis of the different LIS1-bound dynein species reveal insight into the importance of the site^{stalk}-bound LIS1 and support an avidity model, in which having two bindings sites on dynein improves LIS1 binding. This is consistent with data indicating that a Pac1 monomer in yeast can rescue function only if overexpressed[28]. The importance of LIS1-LIS1 binding

is further highlighted by the presence of disease-correlated missense mutations in the LIS1 LisH dimerization domain (*e.g.*, F31S, L43S, W55M)[49–51].

Although our work reveals the likely basis for dynein-Pac1/LIS1 dissociation, we cannot completely discount other changes that might contribute to this process. For example, a previous study found that the N-terminal region of the dynein linker element encounters Pac1 during its powerstroke[27]. One potential hypothesis is that the linker swing may thus partly account for the dissociation (*i.e.*, by knocking it off). However, in contrast to this possibility, we find a dynein with a shortened linker that does not encounter Pac1[27] is sufficient for the dissociation. This is further supported by our 3D classification analysis, which reveals that a straight linker is not necessarily incompatible with LIS1 binding. Finally, given the apparent contact between the tip of the buttress of dynein$^{MT\text{-}U}$ and the site^{stalk}-bound LIS1, the affinity of LIS1 for site^{stalk} is likely also significantly weakened by microtubule-binding.

METHODS

Media and strain construction

Strains are derived from either W303 (for protein purification) or YEF473 (for cell imaging)[53]. We transformed yeast strains using the lithium acetate method[54]. Strains carrying mutations, insertions (*e.g.*, SRS^{CC}), or tagged components were constructed by PCR product-mediated transformation[55], by transforming plasmids with recombination or expression cassettes[2,35], or by mating followed by tetrad dissection. Proper tagging and mutagenesis was confirmed by PCR, and in some cases sequencing. Fluorescent tubulin-expressing yeast strains were generated using plasmids and strategies described previously[56]. Yeast synthetic defined (SD) media was obtained from Sunrise Science Products (San Diego, CA).

Plasmid and BACmid construction

To construct yeast strains expressing SRS^{CC}-containing yeast dynein motor domain fragments (dynein$_{MOTOR}^{MT\text{-}U}$ and dynein$_{MOTOR}^{MT\text{-}B}$), we used PCR-product mediated engineering, or plasmid-based recombination with various engineered pSM01:Dyn1$_{MOTOR}$-3YFP plasmids (generated using Gibson assembly[35,57]; see Table S2 for primers used). The seryl tRNA sythetase coiled-coil (residue 30–96) was amplified from *T. thermophilus* (strain BB8) genomic DNA and integrated into the native *DYN1* gene in yeast to achieve the sequences depicted in Extended Data Figure 1B (note the presence of 4 additional amino acids in the MT-B mutant with respect to MT-U). The pSM01:Dyn1$_{MOTOR}$-3YFP plasmids were generated by amplifying the engineered region from the resulting yeast strains, and all subsequent mutants were engineered into this plasmid (*e.g.*, EQN, KDEE, *etc*), which was digested (with BsaBI/BsiWI; to release the respective dynein open reading frame along with a *TRP1* marker, all of which is flanked with homology arms) and subsequently transformed into *dyn1Δ::HIS3* yeast. The entire cassette is integrated into the *DYN1* locus (resulting in HIS^{-}/TRP^{+} cells), and is the only source of dynein in these cells. Genomic integration was confirmed by growth on selective solid media (one lacking histidine, and another lacking tryptophan), and by PCR.

The human dynein motor domain (residues 1458–4646) was amplified from pbiG1a:6XHis-ZZ-TEV-SNAPf-DHC (codon optimized for insect cells; a gift from A. Carter)[58] and assembled into pFastBac:8His-ZZ-TEV-LIS1-SNAPf (replacing LIS1-SNAPf), generating pFastBac:8His-ZZ-TEV-DHC$_{MOTOR}$. The SRS^{CC} from *T. thermophilus* was engineered into this plasmid to generate the MT-U and MT-B mutants. These plasmids (along with pFastBac:8His-ZZ-TEV-LIS1-SNAPf) were individually transformed into DH10 EMBacY cells (Geneva Biotech, Geneva, Switzerland) according to the manufacturer's protocol. Proper transposition and BACmid generation was confirmed by blue/white screening, and by PCR.

Protein purification

Purification of yeast dynein (wild-type and mutants; ZZ-TEV-dynein$_{331}$-HALO, or ZZ-TEV-6His-GFP-3HA-GST-dynein$_{331}$-HALO, all under the control of the galactose-inducible promoter, *GAL1p*) or Pac1-SNAP was performed as previously described[2,28,59]. Briefly, yeast cultures were grown in YPA supplemented with 2% galactose, harvested, washed with cold water, and then resuspended in a small volume of water. The resuspended cell pellet was drop frozen into liquid nitrogen and then lysed in a coffee grinder (Hamilton Beach). After lysis, 0.25 volume of 4X lysis buffer (1X buffer: 30 mM HEPES, pH 7.2, 50 mM potassium acetate, 2 mM magnesium acetate, 0.2 mM EGTA) supplemented with 1 mM DTT, 0.1 mM Mg-ATP, 0.5 mM Pefabloc SC (concentrations for 1X buffer) was added, and the lysate was clarified at 310,000 x g for 1 hour. The supernatant was then bound to IgG sepharose 6 fast flow resin (Cytiva) for 2–4 hours at 4°C, which was subsequently washed three times in 5 ml lysis buffer, and twice in TEV buffer (50 mM Tris, pH 8.0, 150 mM potassium acetate, 2 mM magnesium acetate, 1 mM EGTA, 0.005% Triton X-100, 10% glycerol, 1 mM DTT, 0.1 mM Mg-ATP, 0.5 mM Pefabloc SC). To fluorescently label the proteins, the bead-bound protein was incubated with either 10 μM JFX646-HaloTag (for the motors) or JF646-SNAP-tag ligand (for Pac1; Janelia Research Campus) for 30–60 minutes at 4°C. The resin was then washed four more times in TEV digest buffer, then incubated in TEV buffer supplemented with TEV protease overnight at 4°C. Following TEV digest, the protein-containing supernatant was collected using a spin filtration device, aliquoted, flash frozen in liquid nitrogen, and stored at −80°C.

Human proteins (LIS1-SNAP, or motor domains) were expressed and purified from insect cells (ExpiSf9 cells; Life Technologies) as previously described with minor modifications[3,6,18,58]. Briefly, 4 ml of ExpiSf9 cells at 2.5 x 10^6 cells/ml, which were maintained in ExpiSf CD Medium (Life Technologies), were transfected with 1–9 μg of bacmid DNA using ExpiFectamine (Life Technologies) according to the manufacturer's instructions. 4–8 days following transfection, the cells were pelleted, and 1–2 ml of the resulting supernatant (P1) was used to infect ~150 ml of ExpiSf9 cells (5 x 10^6 cells/ml). Approximately 65 hours later, the cells were harvested (2000 x g, 20 min), washed with human dynein lysis buffer (50 mM HEPES, pH 7.4, 100 mM NaCl, 10% glycerol, 1 mM DTT, 0.1 mM Mg-ATP, 1 mM PMSF; note ATP was omitted for LIS1 purification), pelleted again (1810 x g, 20 min), and resuspended in an equal volume of same. The resulting cell suspension was drop frozen in liquid nitrogen and stored at −80°C. For protein purification, 30 ml of additional human dynein lysis buffer supplemented with cOmplete

protease inhibitor cocktail (Roche) was added to the frozen cell pellet, which was then rapidly thawed in a 37°C water bath prior to incubation on ice. Cells were lysed in a dounce-type tissue grinder (Wheaton) using 50–60 strokes. Subsequent to clarification at 310,000 x g for 1 hour, the supernatant was applied to 2 ml of IgG sepharose fast flow resin (GE) pre-equilibrated in human dynein lysis buffer, and incubated at 4°C for 3–5 hours. Beads were then washed 3 times with with 5–10 ml of human dynein lysis buffer, and 2 times with 5–10 ml of human dynein TEV buffer (50 mM Tris pH 7.4, 150 mM potassium acetate, 2 mM magnesium acetate, 1 mM EGTA, 10% glycerol, 1 mM DTT, 0.1 mM Mg-ATP; note ATP was omitted for LIS1 purification). The beads were incubated with TEV protease overnight at 4°C. The next morning, the recovered supernatant was collected, concentrated, aliquoted, flash frozen, then stored at −80°C. Note that protein used for cryo-EM was processed directly without freezing. LIS1-SNAP required a gel filtration step to improve purity for mass photometry. To this end, the TEV eluate was injected on to a Superdex 200 10/300 equilibrated in TEV buffer (without ATP). Peak fractions were pooled, concentrated, aliquoted, snap frozen, and stored at −80°C.

Dynein ATPase assays

ATPase activities were determined using the EnzChek phosphate assay kit (Life Technologies). Assays were performed in motility buffer (30 mM HEPES pH 7.2, 50 mM potassium acetate, 2 mM magnesium acetate, 1 mM EGTA, 1 mM DTT) supplemented with 2 mM MgATP, with or without 2 μM taxol-stabilized microtubules, 5 nM 6His-GST-dynein$_{331}$ (wild-type or mutants). Reactions were initiated with the addition of dynein, and the absorbance at 360 nm was monitored by a spectrophotometer for 10–20 min. Background phosphate release levels (presumably from microtubules) for each reaction were measured for 5 min before addition of dynein to account for any variation as a consequence of differing microtubule concentrations, and were subtracted out from each data point.

Dynein microtubule-binding assays

Flow chambers constructed using slides and plasma cleaned and silanized coverslips attached with double-sided adhesive tape were coated with anti-tubulin antibody (8 μg/ml, YL1/2; Accurate Chemical & Scientific Corporation) then blocked with a mixture of 1% Pluronic F-127 (Fisher Scientific) and 1 mg/ml κ-casein. Taxol-stabilized microtubules assembled from porcine tubulin (Cytoskeleton) were introduced into the chamber. After microtubules were adhered to the cover glass, 50 nM dynein$_{MOTOR}$ fragments (wild-type or mutant) diluted in TEV buffer were flowed into the chambers. After a brief incubation (2–5 minutes), images were acquired at room temperature using a 1.49 NA 100X objective on a total internal reflection fluorescence (TIRF) Ti-E inverted microscope (Nikon), equipped with a SOLA SM II LE LED light engine (Lumencor), a motorized filter cube turret, and an iXon X3 DU897 cooled EM-CCD camera (Andor). A 640 nm laser (Nikon) was used along with a multi-pass quad filter cube set (C-TIRF for 405/488/561/638 nm; Chroma) and an emission filter mounted in a filter wheel (700/75 nm; Chroma) to image dynein$_{MOTOR}$-HaloTag^{JFX646}.

Live cell imaging experiments

Cells were grown to mid-log phase in SD media supplemented with 2% glucose, and mounted on agarose pads. Images were collected at room temperature using a 1.49 NA 100X objective on a Ti-E inverted microscope equipped with a Ti-S-E motorized stage (Nikon), piezo Z-control (Physik Instrumente), a SOLA SM II LE LED light engine (Lumencor), a motorized filter cube turret, and an iXon X3 DU897 cooled EM-CCD camera (Andor). The microscope system was controlled by NIS-Elements software (Nikon). Step sizes of 0.5 μm (for Bik1–3mCherry quantitation) or 1 μm (for dynein quantification) were used to acquire 2-μm-thick Z-stack images. Sputtered/ET filter cube sets (Chroma Technology) were used for imaging mTurquoise2 (49001), GFP (49002), YFP (49003), and mCherry (49008) fluorescence. Images were analyzed using FIJI/ImageJ. Plus end and cortical foci were scored (frequency and intensity) from maximum-intensity projected timelapse movies. All foci were scored from timelapse movies. Those foci observed moving coincident with the ends of microtubules were scored as plus end-associated, while those that appeared to be statically associated with the cortex for ≥3 frames were scored as cortically-associated. Intensity values plotted throughout are background corrected as follows: a 3x3 box drawn around each focus was used to measure signal, while the same size box was drawn around an adjacent region in the cytoplasm to measure background, which was subtracted from the signal. For Figure 1, all dynein and Pac1 intensity values were normalized to the mean values (for each replicate) of plus end-associated dynein and Pac1, respectively, in wild-type cells (each set to 1). For Figure 7E and F, all intensity values were normalized to the mean values (for each replicate) for $dynein_{MOTOR}^{MT\text{-}U}$-3YFP (set to 1).

Analytical size exclusion chromatography

To assess $dynein_{MOTOR}$-Pac1 binding, equal concentrations of purified motor proteins (~8 μg $dynein_{MOTOR}$-$HaloTag^{JFX646}$) were first incubated in the indicated nucleotide (3 mM each) for 10 minutes on ice, followed by addition of Pac1-$SNAP^{JFX646}$ (~2 μg; final concentrations of each were between 400–600 nM each). Following a 10 minute incubation on ice, the mixture was injected on to a Superdex 5/150 using an AKTA Pure. Fractions with JFX646-labeled proteins were separated by SDS-PAGE, which were subsequently scanned using a Typhoon gel imaging system (FLA 9500). FIJI was used to determine background-subtracted band intensity.

Mass photometry

With the exception of LIS1-SNAP, all purified proteins were used directly for mass photometry without additional purification steps. LIS1-SNAP required an additional gel filtration step to remove higher molecular weight species (as determined by mass photometry; see above). All proteins were initially diluted to 500 nM in assay buffer (50 mM Tris, pH 8.0, 150 mM potassium acetate, 2 mM magnesium acetate, 1 mM EGTA, 1 mM DTT) with or without added nucleotide (1 mM of each, as indicated in figures), and then subsequently diluted to 50 nM in same. 3 μl of each was then mixed 1:1 (to 25 nM of each), incubated for 1–2 minutes, and then diluted 1:5 on the stage (2.5 μl of mixed protein + 10 μl same buffer with or without nucleotide) to 5 nM final immediately prior to image acquisition. For apo conditions, residual ATP from the protein preparation was

depleted using apyrase by mixing 4.5 µl of 500 nM protein with a 0.5 µl of apyrase (NEB), and incubating for 30 minutes at room temperature. 1 minute movies were acquired using Refeyn MP, and all images were processed and analyzed using Discover MP. Calibration was performed with beta-amylase and thyroglobulin.

Cryo-EM grid preparation

Purified proteins (as described above) were applied to a TSKgel G4000SWXL column pre-equilibrated with 50 mM Tris pH 7.4, 150 mM potassium acetate, 2 mM magnesium acetate, 1 mM EGTA, 1 mM DTT, and 0.1 mM Mg-ATP. Peak fractions were pooled and 1 mM Mg-ATP with (for MT-U proteins) or without (for MT-B) 1 mM Na_3VO_4 was immediately added. Protein quality was examined by negative staining microscopy. Glycerol was added to a final concentration of 10%, aliquots were flash-frozen in liquid nitrogen, and stored at −80 °C. For initial cryo-EM analysis of the human dynein MT-B mutant in ATP buffer (50 mM Tris pH 7.4, 150 mM potassium acetate, 2 mM magnesium acetate, 1 mM EGTA, 1 mM DTT, 1 mM Mg-ATP), we found that a high concentration (> 5 mg/ml) of protein was required for the protein to enter the open holes of a plasma cleaned QUANTIFOIL Au R2/1 300-mesh grids (Extended Data Fig. 4A). To reduce the sample concentration during cryo-EM grid preparation for human dynein MT-U mutant in buffer supplemented with ATP and Vi (50 mM Tris pH 7.4, 150 mM potassium acetate, 2 mM magnesium acetate, 1 mM EGTA, 1 mM DTT, 1 mM Mg-ATP and 1 mM Na_3VO_4), we coated QUANTIFOIL Cu R2/1 300-mesh grids with graphene-oxide (GO) layers, as previously reported[60]. 4 µl of the MT-U mutant with or without human LIS1 at 0.2–0.4 mg/ml were applied to the graphene oxide-coated side of freshly prepared GO-grids (Extended Data Fig. 4F and K), followed by a 4 s wait time, 3–6 s blot time, 4 blot force, and subsequent freezing in liquid ethane using a Vitrobot Mark IV unit (FEI). The Vitrobot chamber was maintained at close to 95% humidity at 4°C.

The MT-B and MT-U alone data were collected at the Yale ScienceHill-Cryo-EM facility using a Glacios microscope (Thermo Fisher Scientific) operated at 200 keV. The images were collected with a K2 direct electron detector (Gatan) operating in super-resolution mode, at a nominal magnification of 36,000X, corresponding to a pixel size of 1.149 Å. Data collection was automated by SerialEM software[61] with a defocus range of −1.5 µm to −2.7 µm. In total, 3035 movies for MT-B and 3065 movies for MT-U were collected and each movie was dose-fractionated to 40 frames with a total dose of 40 e-/Å^2 (Extended Data Fig. 4, Table 1).

The MT-U + LIS1 data was collected at the Laboratory for BioMolecular Structure (LBMS) using a Titan Krios microscope (Thermo Fisher Scientific) operated at 300 keV and equipped with a K3 detector and a BioQuantum energy filter (Gatan) with a slit width of 15 eV. Data collection was automated by EPU software with a defocus range of −1.5 µm to −2.7 µm, and all movies were recorded in a super-resolution mode at a nominal magnification of 105,000X corresponding to a pixel size of 0.825 Å. Each movie was dose-fractionated to 50 frames with a total dose of 50 e-/Å^2. A total of 5183 movies were collected (Extended Data Fig. 4, Table 1).

Cryo-EM image processing

Cryo-EM data processing workflows are outlined in Extended Data Figure 4. Recorded movies were pre-processed using cryoSPARC Live[62] including patch motion correction and patch CTF estimation. Exposures were manually curated and micrographs without graphene oxide were removed.

For the MT-B dataset (Extended Data Fig. 4A–E), Topaz picker[63] was used for particle picking. In total, 250,463 particles were extracted with a box size of 360 with a pixel size of 1.149 Å. Multiple rounds of 2D classification were performed to filter the particles. Good particles were used for *ab-initio* reconstruction in cryoSPARC. The reconstructed volume was used for several rounds of heterogenous refinement followed by 2D classification. Finally, 44,752 particles were selected and subjected to non-uniform refinement[64] followed by two rounds of global and local CTF refinement. A 3.4 Å map was obtained as evaluated using a GSFSC criterion of 0.143.

For the MT-U + LIS1 dataset (Extended Data Fig. 4F–J), Blob picker in cryoSPARC was used for particle picking. An initial 1,400,918 particles were extracted with a box size 500 and binned to 360 box size, resulting in a pixel size of 1.149 Å. The MT-B map was low-passed to 30 Å and used for heterogenous refinement. After several rounds of heterogenous refinement followed by 2D classification, 182,694 particles were selected and subjected to non-uniform refinement. While the dynein motor region was resolved at better resolution, the LIS1 density appeared to be smeared, suggesting flexibility for LIS1 binding. Before performing 3D classification focusing on LIS1 density, we used a mask around the motor region to perform two rounds of global, local CTF refinement, followed by local refinement to better estimate high-order CTF terms and each particle's local defocus value. This yielded a 2.8 Å map of the motor region. We then used a mask around the AAA3-AAA5–2 LIS1 density for local 3D classification without alignment in cryoSPARC. After classification, 3 major classed were obtained: 1 LIS1 bound (66,212 particles, 36.2%), "1.5" LIS1 bound (62, 910 particles, 34.4%) and 2 LIS1 bound (53,572 particles, 29.3%; see Extended Data Fig. 9). The 2 LIS1 bound class was subjected to global refinement (motor with 2 LIS1) and local refinement (AAA3-AAA5 with 2 LIS1), yielding a 3.2 Å and 3.3 Å map, respectively.

For the MT-U alone dataset (Extended Data Fig. 4K–O), a similar strategy was used. 729,028 particles picked by the Blob picker were extracted with a box size of 360. Multiple rounds of heterogenous and 2D classification were used to clean the particles. Finally, 201,717 particles were subjected to non-uniform refinement. Two rounds of global and local CTF refinement followed by local refinement allowed us to obtain a 2.9 Å map.

Local resolution estimation of all maps was performed in cryoSPARC. Directional anisotropy analysis of all maps was performed using 3DFSC[65] implemented in cryoSPARC.

Model building and refinement

A previously reported human dynein motor structure[3] (PDB: 5NUG) was used as an initial model. Individual domains (linker, AAA large, AAA small) were docked into the cryo-EM map as rigid bodies using UCSF ChimeraX[66]. After docking, Namdinator[67], a molecular dynamics flexible fitting tool, was used to further fit the model into the cryo-EM

map. The model was then manually inspected and adjusted in COOT v0.9.5[68,69]. The high-resolution cryo-EM map together with our biochemical assay allowed us to confidently assign nucleotides to each pocket. For example, by adjusting the contour level, we could see the separation of vanadate, Mg^{2+}, and ADP in the MT-U AAA1 pocket. Our vanadate-mediated photocleavage assay also indicated that vanadate binds to the MT-U AAA1 pocket. These two pieces of evidence allowed us to build ADP-Vi into the MT-U AAA1 pocket.

To build the model for human LIS1, the predicted structure from AlphaFold[70] database was used as the initial model. The positions of two LIS1 were determined using a previously reported yeast dynein-Pac1 structure[39] (PDB: 7MGM). All models were iteratively refined using Phenix real-space refinement 1.19.2_4158[71] and manual rebuilding in COOT. The quality of the refined model was analyzed by MolProbity integrated into Phenix[72] with statistics reported in Table 1. Figures were prepared using UCSF ChimeraX[66].

Molecular dynamics simulation and interface energy calculations—The cryo-EM structure of the MT-U-2 LIS1 complex was prepared before modeling and simulations in Charmm-GUI[73]. The large-scale Atomic/Molecular Massively Parallel Simulator was applied for the simulations[74]. Periodic boundary conditions were used to produce a series of proteins. Amber10:EHT force field (https://infoscience.epfl.ch/record/121435/files/Amber10i.pdf) was used to simulate proteins. Water molecules were simulated using the rigid SPC/E force field[75] whereas the SHAKE algorithm[76] was used to keep the water molecules rigid throughout the entire simulation. Lennard-Jones 12– 6 term[77] is used to describe the short-range interactions and the cutoff distance was 12 Å. The particle-particle/particle-mesh method with a precision value of 10^{-6} was adopted to estimate long-range electrostatic interactions[78]. First, we ran the energy minimization for the whole system. Next, the simulations were carried out at 25°C using a canonical NVT ensemble, where the temperature was controlled by the Nosé-Hoover thermostat[79]. Then NPT ensemble was performed in production phase where the target pressure and temperature were 1 atm and 25°C respectively. Default tether restraints from LAMMPS were applied to the system.

Protein models after in silico mutations underwent the same preparation procedure. Interface energy was calculated in the production phase. The interface energy calculation between contacting residue pairs was processed. The proximity threshold was set to 12 Å. Atoms separated by more than this distance were not considered to be interacting. Six types of contacts were identified: hydrogen bonds, metal, ionic, arene, covalent and Van der Waals distance interactions.

Figure Preparation—Figures and plots were prepared using GraphPad Prism 9.0, MP Discover (for mass photometry data), FIJI/ImageJ (for light microscopy images), USCF ChimeraX 1.4, and Adobe Illustrator 27.1.1.

Statistics and Reproducibility—All data were collected from at least two independent replicates (independent protein preparations, or cell cultures, for *in vitro* and *in vivo* experiments, respectively). All phenotypes were also validated in at least 2 biological replicates for *in vivo* experiments. The values from each independent replicate showed similar results. T-tests were performed using GraphPad Prism. Statistical significance was

determined using an ANOVA with Dunnett's multiple comparison test, or by calculating Z scores using the following formula:

$$Z = \frac{(\hat{p}_1 - \hat{p}_2)}{\hat{p}\left(1 - \hat{p}\right)\left(\frac{1}{n_1} + \frac{1}{n_2}\right)}$$

where:

$$\hat{p} = \frac{y_1 + y_2}{n_1 + n_2}$$

Z scores were converted to two-tailed P values using an online calculator.

Extended Data

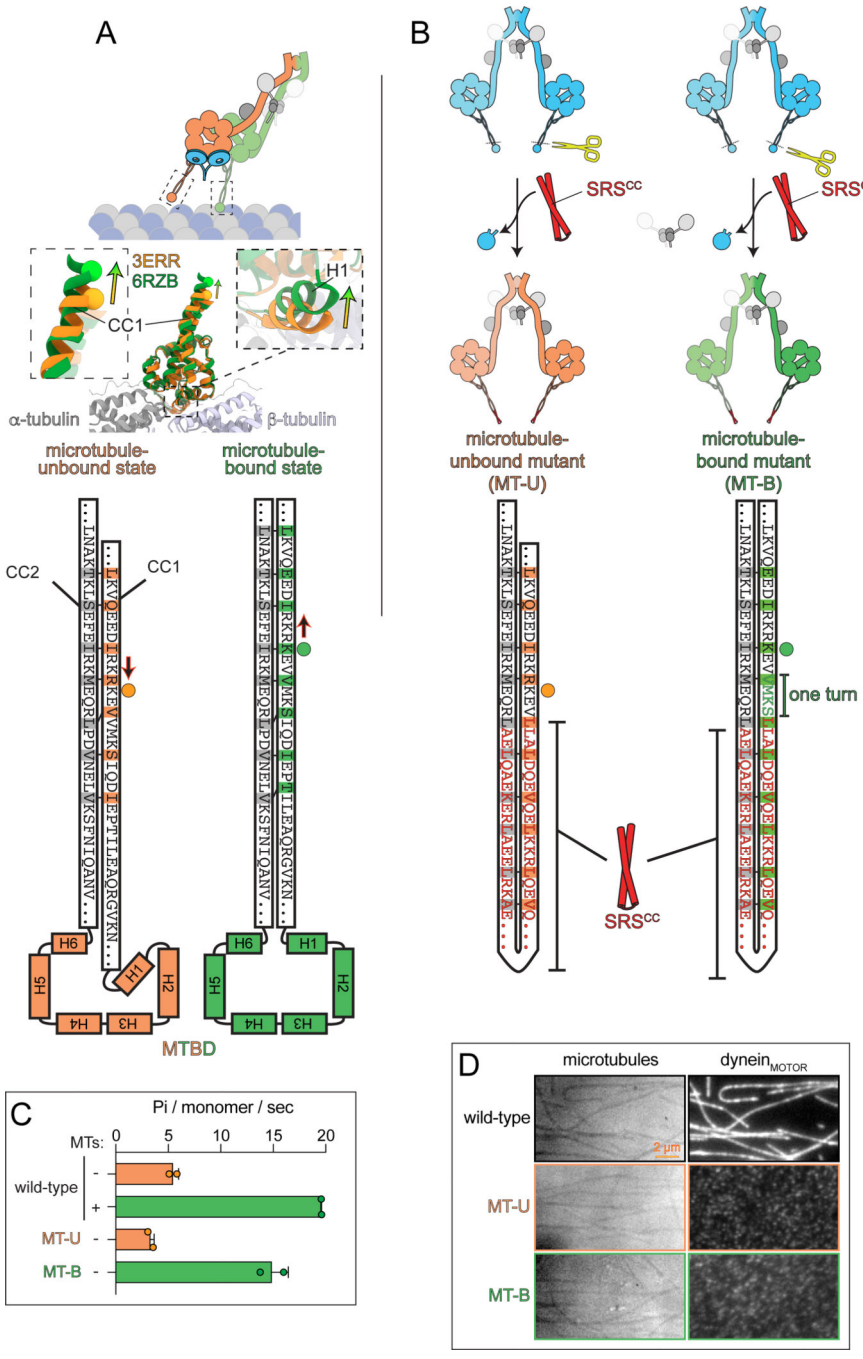

Extended Data Figure 1. Design strategy and validation of microtubule-bound and -unbound dynein mutants.

(A) Cartoon and structural depiction of conformational change that takes place at the coiled-coil (CC) stalk and microtubule-binding domain (MTBD) upon microtubule binding. Comparison of a high resolution microtubule-bound dynein MTBD (6RZB)[30] and a crystal structure of a microtubule unbound MTBD (3ERR)[32] reveals an upward shifting of helix 1 (H1) as a result of microtubule binding. This results in a consequent upward shift

of CC1 with respect to CC2. (B) Design strategy to generate constitutive microtubule-unbound and -bound dynein mutants. The stable coiled-coil from seryl tRNA synthetase (SRS^{CC}) was used to replace the entire dynein MTBD plus short regions of CC1 and CC2. The MT-B mutant has 4 additional residues in CC1 with respect to the MT-U mutant (corresponding to one helix turn), resulting in a presumed upward shift of CC1 compared to CC2. (C) Plot (mean ± SD, along with individual data points) depicting ATPase levels for artificially dimerized dynein motor domain fragments (GST-$dynein_{MOTOR}$; n = 2 independent replicates for each). Note the MT-U mutant closely reflects the wild-type dynein motor in the absence of microtubules, while the MT-B mutant matches that of wild-type plus a saturating concentration of microtubules (2 μM)[59]. (D) Representative images (fluorescence for $dynein_{MOTOR}$ fragments, and interference reflection microscopy for microtubules) showing the ability of wild-type, but not $dynein^{MT-U}$ or $dynein^{MT-B}$, to bind microtubules (images are representative of 2 independent replicates). Coverslip-immobilized microtubules were incubated with 50 nM of indicated $dynein_{MOTOR}$ fragments (labeled via C-terminal $HaloTag^{JFX646}$) prior to imaging.

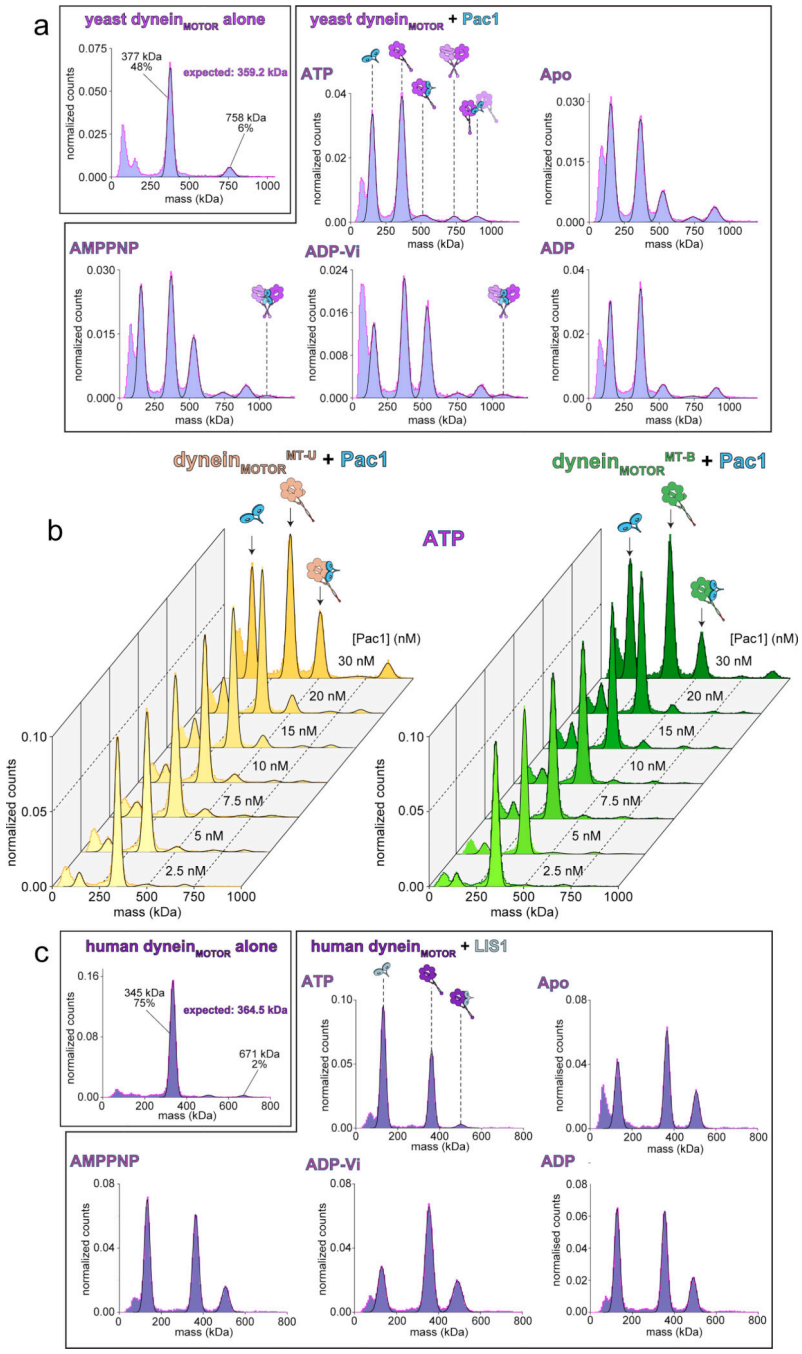

Extended Data Figure 2. Additional mass photometric analysis of Pac1- and LIS1-dynein^{MOTOR} binding.

(A) Histograms of mass photometry analysis depicting relative dynein$_{MOTOR}$-Pac1 complex formation in the presence of a fixed concentration of each motor (25 nM) and increasing concentrations of Pac1 (as indicated). Note the higher fraction of dynein$_{MOTOR}^{MT-U}$-Pac1 complex formation with respect to dynein$_{MOTOR}^{MT-B}$-Pac1 at every concentration. (B and C) Representative mass histograms for the wild-type yeast (B) and human (C) dynein$_{MOTOR}$ proteins with and without Pac1 or LIS1 with different nucleotides, as indicated (see Figure

3 and Methods). Cartoon depictions above each peak in the ATP panel indicates the likely dynein$_{MOTOR}$-Pac1 or LIS1 complex contained therein.

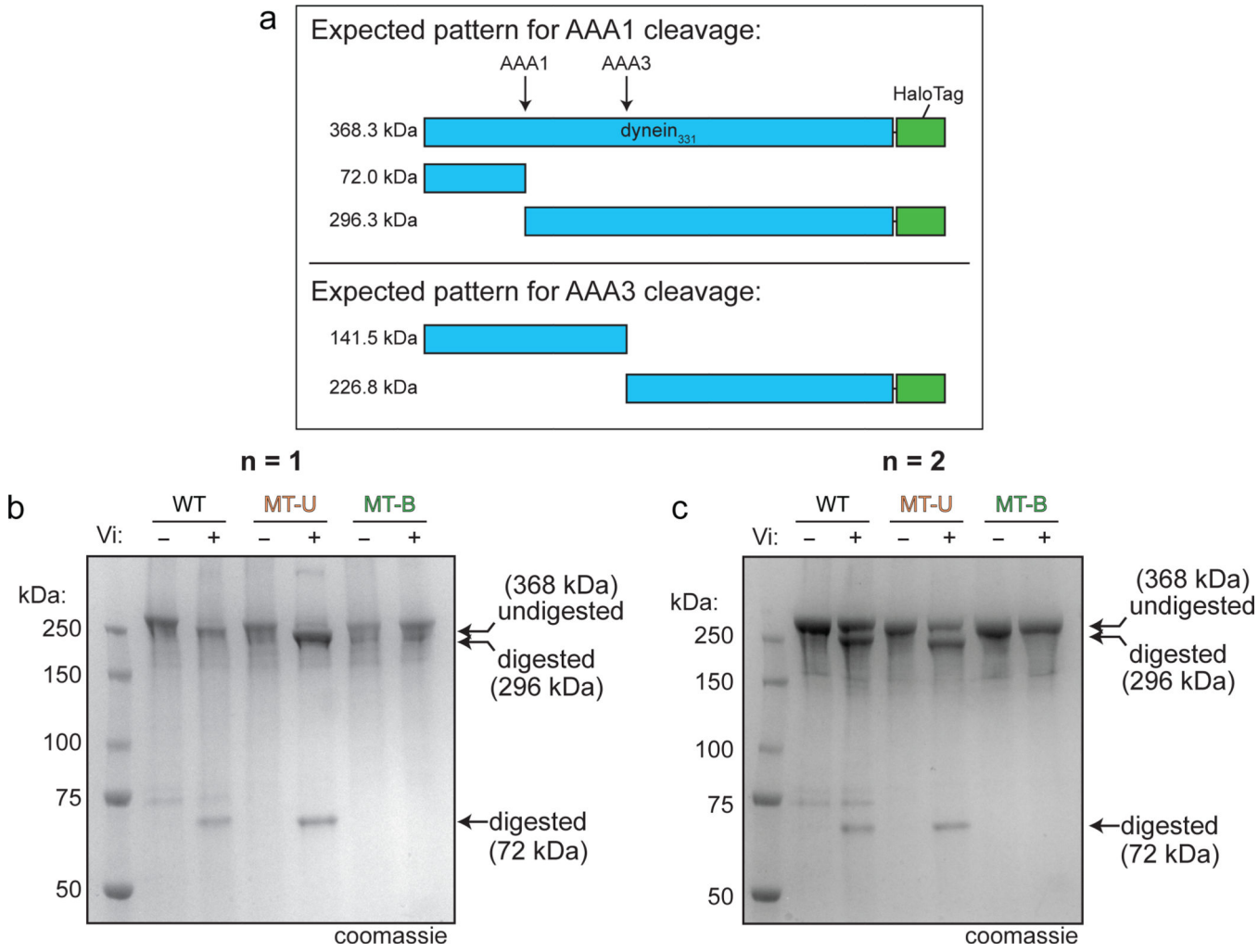

Extended Data Figure 3. Vanadate-mediated photocleavage assay, and the role of ATP binding and hydrolysis in dynein-Pac1 binding.

(A) Schematic depicting expected vanadate-mediated photocleavage if vanadate were bound to AAA1 (top) or AAA3 (bottom). (B and C) Two independent replicates of photocleavage assay. Purified indicated dynein$_{MOTOR}$ fragments were incubated with 3 mM ATP with or without 3 mM vanadate, exposed to ultraviolet light (254 nm) for 1 hour, and then analyzed by coomassie-stained SDS-PAGE.

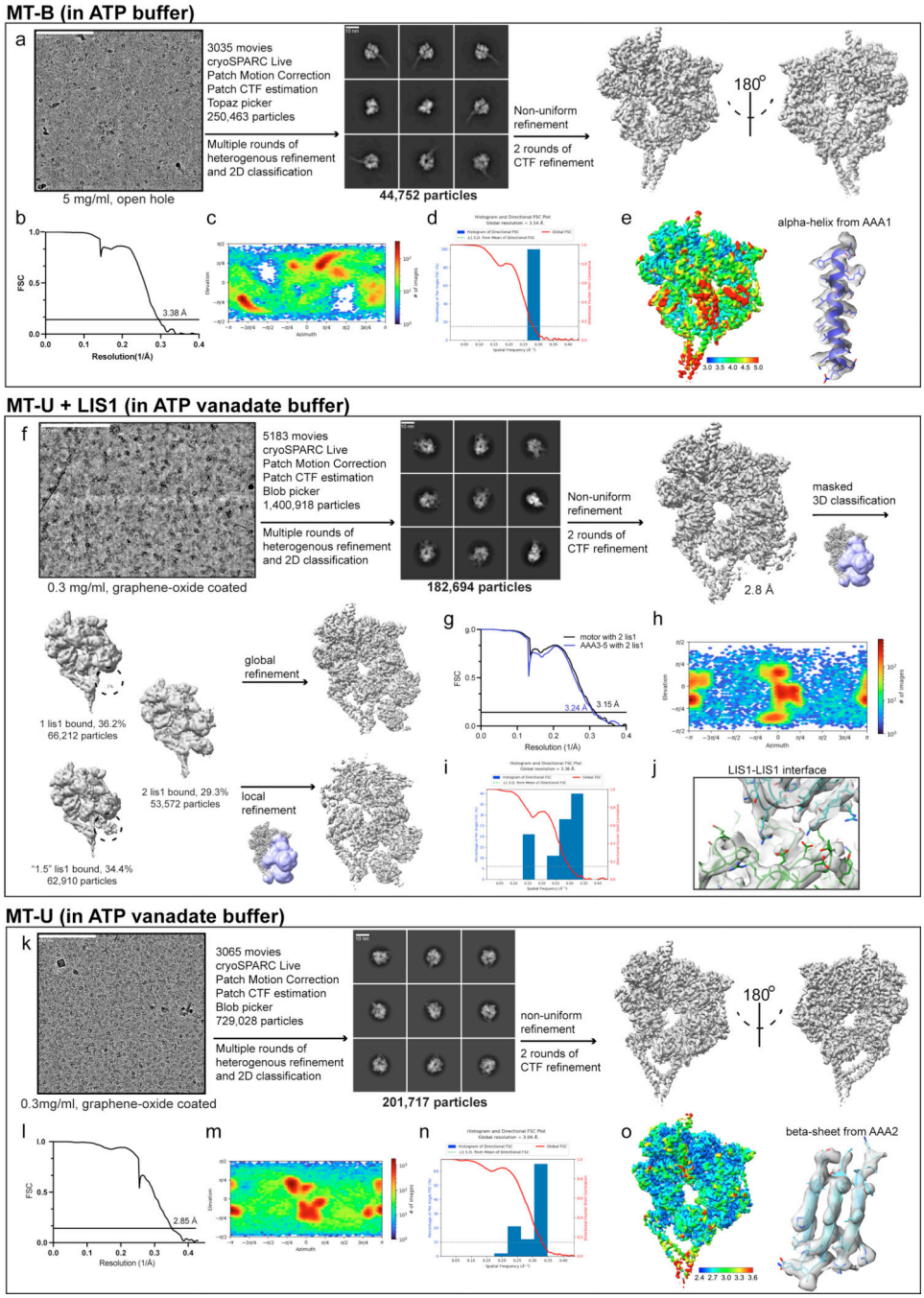

Extended Data Figure 4. Cryo-EM data processing flowchart.

(A) Cryo-EM workflow of MT-B in the presence of ATP (details in methods). (B) FSC curves with the gold standard threshold of 0.143 for MT-B. (C - D) Particle distribution plot and 3D FSC analysis of MT-B. (E) Local resolution analysis of MT-B and representative cryo-EM densities. (F) Cryo-EM workflow of MT-U with LIS1. (G) FSC curves with the gold standard threshold of 0.143. (H - I) Particle distribution plot and 3D FSC analysis of MT-U + LIS1 in the presence of ATP and Vi. (J) Local resolution analysis and representative cryo-EM densities of the LIS1-LIS1 interface. (K) Cryo-EM workflow of MT-U alone in the

presence of ATP and Vi. (L) FSC curves with the gold standard threshold of 0.143. (M - N) Particle distribution plot and 3D FSC analysis of MT-U. (O) Local resolution analysis and representative cryo-EM densities.

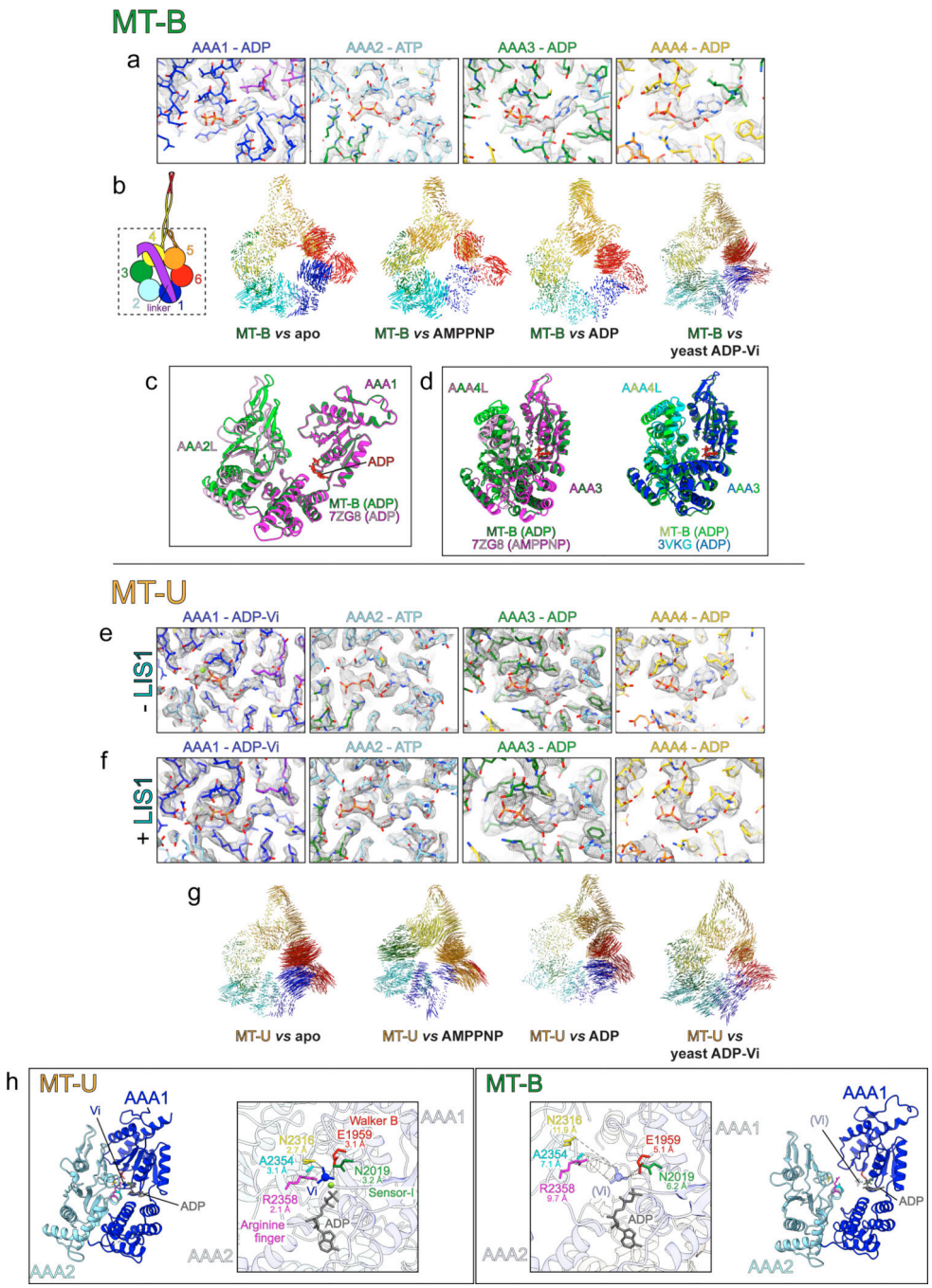

Extended Data Figure 5. Additional analysis of human MT-U and MT-B cryo-EM structures.
(A) Stick representations of the dynein$_{MOTOR}^{MT-B}$ AAA sites showing the nucleotide electron density (the center of each image) and surrounding residues (residues are color-coded as shown in panel B schematic). (B) Vector maps depicting pairwise alpha carbon

interatomic distances between the dynein$_{MOTOR}^{MT-B}$ with the following: apo yeast dynein, AMPPNP-bound yeast dynein (4W8F), ADP-bound *Dictyostelium discoideum* dynein (3VKG), ADP-Vi and Pac1-bound yeast dynein (7MGM)[37,40,80,82]. Structures were globally aligned after removal of the linkers. (C) AAA1-AAA2L domains from dynein$_{MOTOR}^{MT-U}$ (shades of green) and the native microtubule-bound dynein-1 (magenta and pink) overlaid to depict the high degree of structural similarity. The two were locally aligned using AAA1. (D) AAA3-AAA4L domains from dynein$_{MOTOR}^{MT-U}$ (shades of green) overlaid with either the native microtubule-bound dynein-1 (left, magenta and pink) or the ADP-bound *Dictyostelium discoideum* dynein (right, blue and green). (E and F) Stick representations of the LIS1-unbound (E) or bound (F) dynein$_{MOTOR}^{MT-U}$ AAA sites showing the nucleotide electron density and surrounding residues (residues are color-coded as shown in panel B schematic). (G) Vector maps depicting pairwise alpha carbon interatomic distances between the LIS1-bound dynein$_{MOTOR}^{MT-U}$ with those described for panel B. Structures were globally aligned after removal of the linkers. (H) AAA1-AAA2L domains from dynein$_{MOTOR}^{MT-U}$ (left) and dynein$_{MOTOR}^{MT-B}$ (right) with residues of dynein$_{MOTOR}^{MT-U}$ contacting the Vi highlighted (E1959, Walker B; N2019, Sensor-I; R2358, arginine finger; N2316; A2354;). Distances between these residues and the Vi (or, for the dynein$_{MOTOR}^{MT-B}$ structure, between them and where the Vi would be) are indicated.

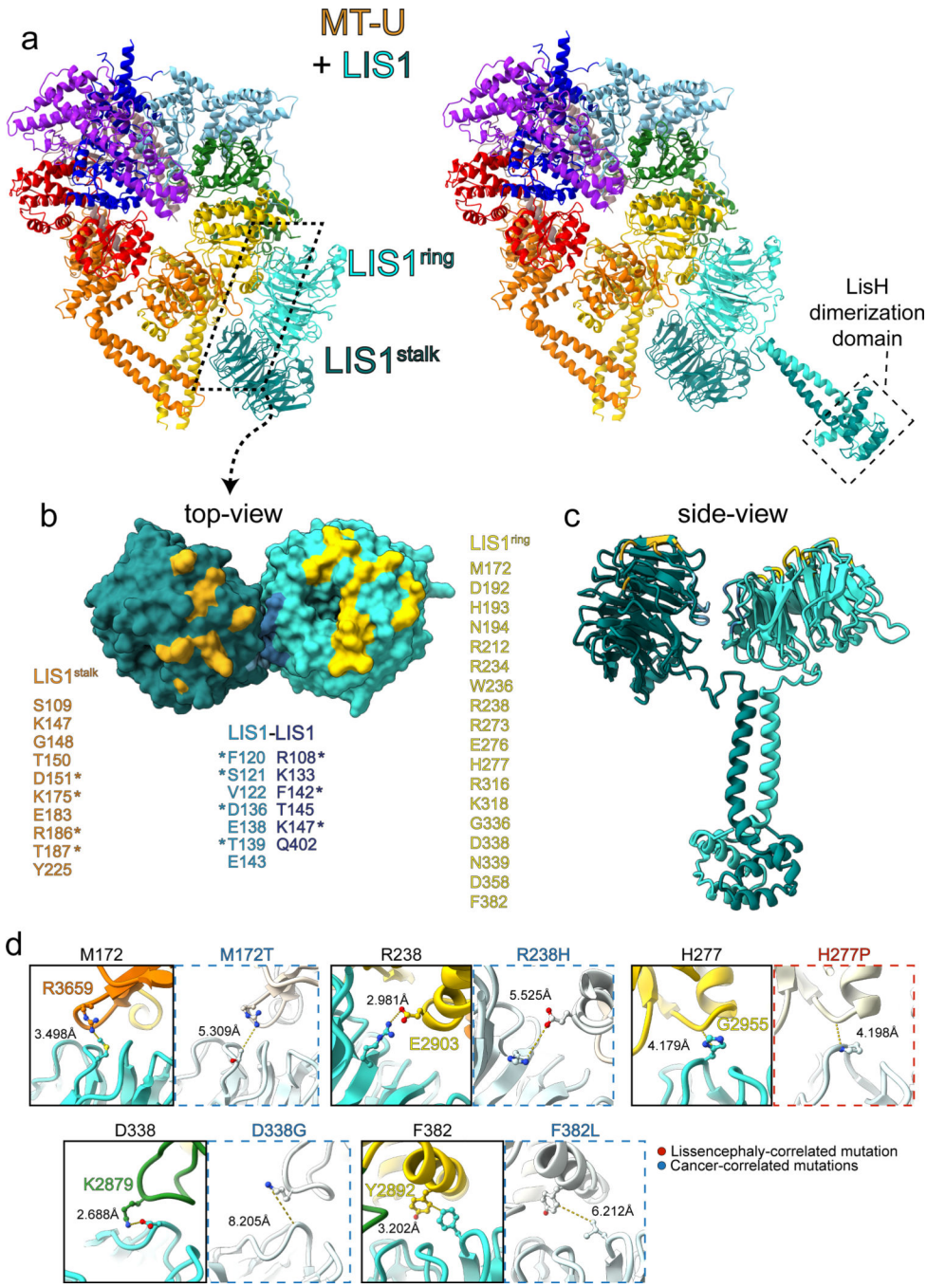

Extended Data Figure 6. Additional analysis of LIS1-bound dynein$_{MOTOR}^{MT-U}$ structure.

(A) 2 LIS1-bound dynein$_{MOTOR}^{MT-U}$ structure with domains colored as shown in Figure 5 (left) and the same shown with the a full-length LIS1 homodimer, with the N-terminal dimerization domain modeled. The LIS1 N-terminal dimer model was generated using a combination of AlphaFold prediction[70] and a previous crystal structure, 1UUJ[83]. The structure was manually adjusted in COOT. (B) View of LIS1 homodimer surface that contacts site^{stalk} (teal) and site^{ring} (cyan). Residues listed and indicated in different colors on the structure are those that make direct contact with dynein or LIS1. Residues with "*"

are those identified in a recent study to make contact with wild-type human dynein[41]. (C) Side-view of full-length LIS1 homodimer model with residues colored as in panel B. (D) Results of molecular dynamics simulation from Figure 5G depicting change in interatomic distances in residues mediating contacts between LIS1 and dynein as a consequence of indicated mutations.

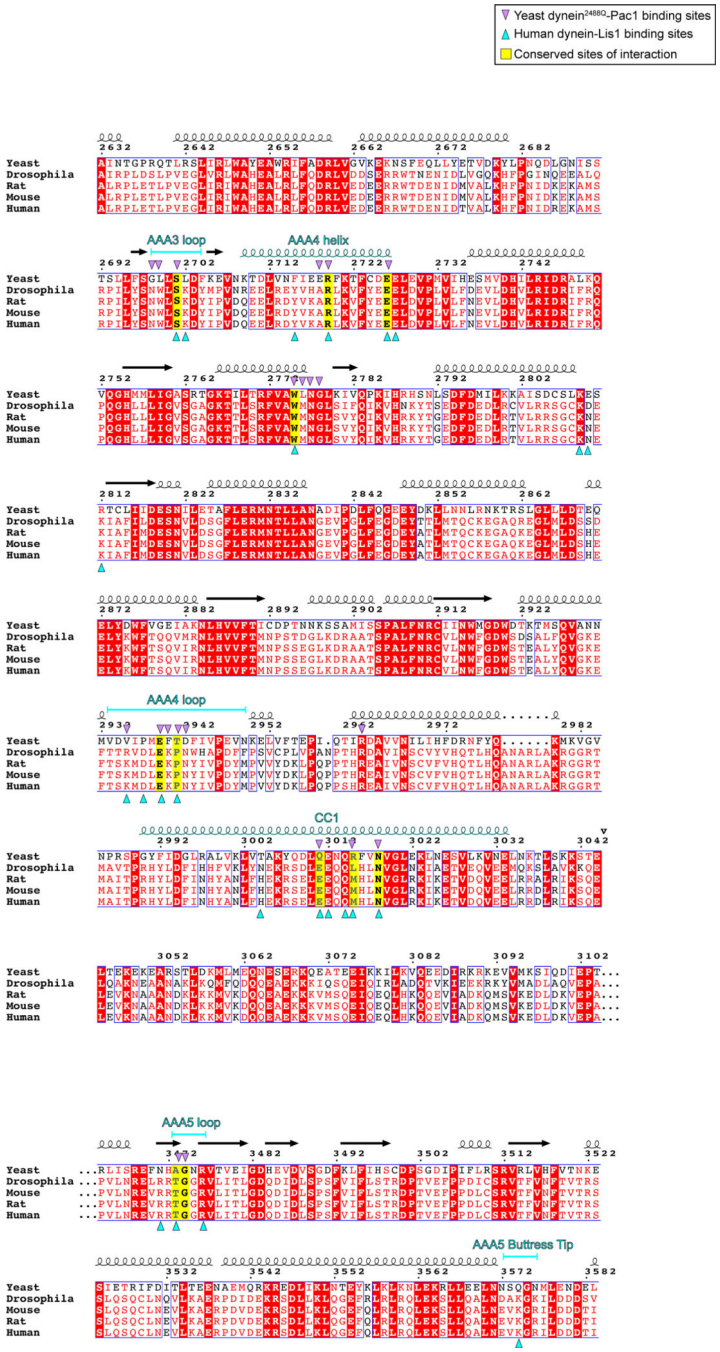

Extended Data Figure 7. Sequence alignment of Pac1 and LIS1-binding regions within dynein.

Numbering corresponds to yeast dynein (Dyn1) sequence. Secondary structure indicated with cartoon helices (for alpha-helices) and arrows (for beta-strands).

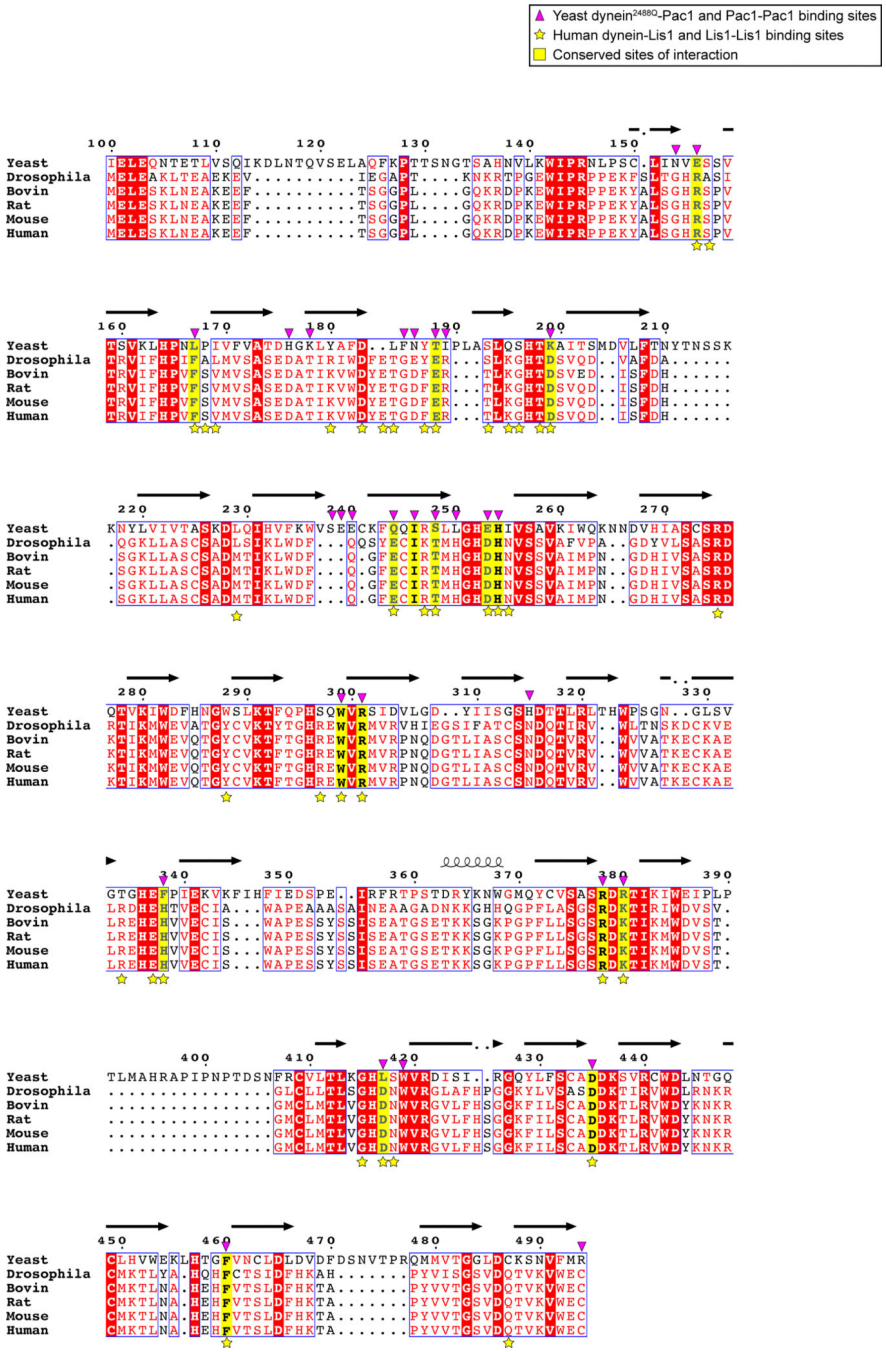

Extended Data Figure 8. Sequence alignment of dynein-binding regions within LIS1 and homologs.

Numbering corresponds to yeast Pac1 sequence. Secondary structure indicated with cartoon helices (for alpha-helices) and arrows (for beta-strands).

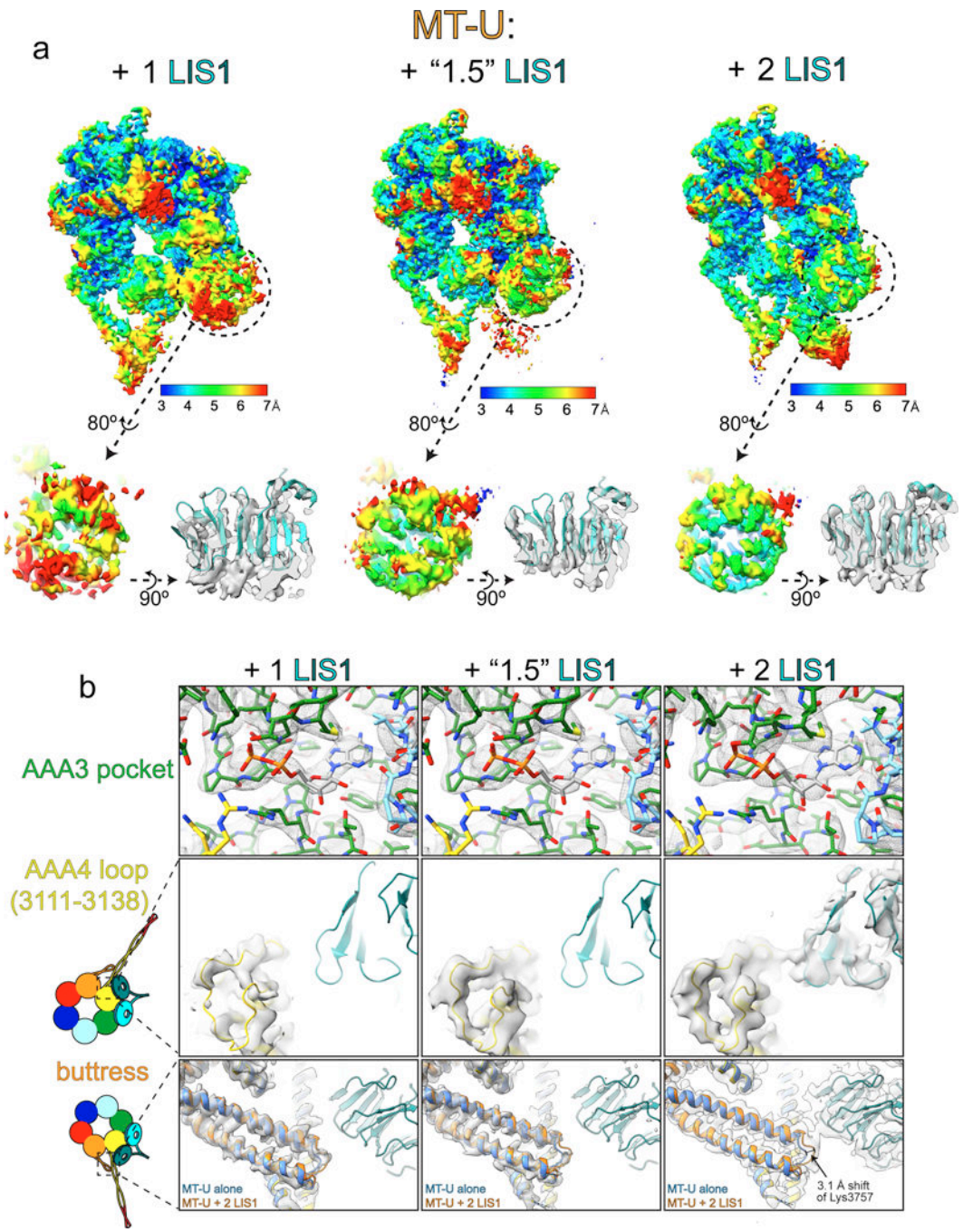

Extended Data Figure 9. 3D classification analysis of LIS1-bound dynein$_{MOTOR}^{MT-U}$ structures.

(A) The three classes of LIS1-bound dynein (shown with a rotated close-up view of LIS1^{ring}) are shown with local resolution indicated by color. Note the significant increase in resolution and map quality for LIS1^{ring} for the "1.5" and 2 LIS1-bound dyneins. (B) Close-up views of the indicated regions of the LIS1-bound dynein$_{MOTOR}^{MT-U}$ structure. Note all three structures have clear density for ADP at AAA3 (top), and there is an improvement in local resolution for the AAA4 loop (middle) and the buttress for the "1.5"

and 2 LIS1-bound structures. EM densities of each 3D class are shown along with models of dynein$_{MOTOR}^{MT-U}$ and dynein$_{MOTOR}^{MT-U}$ + 2 LIS1 for comparison in bottom two rows.

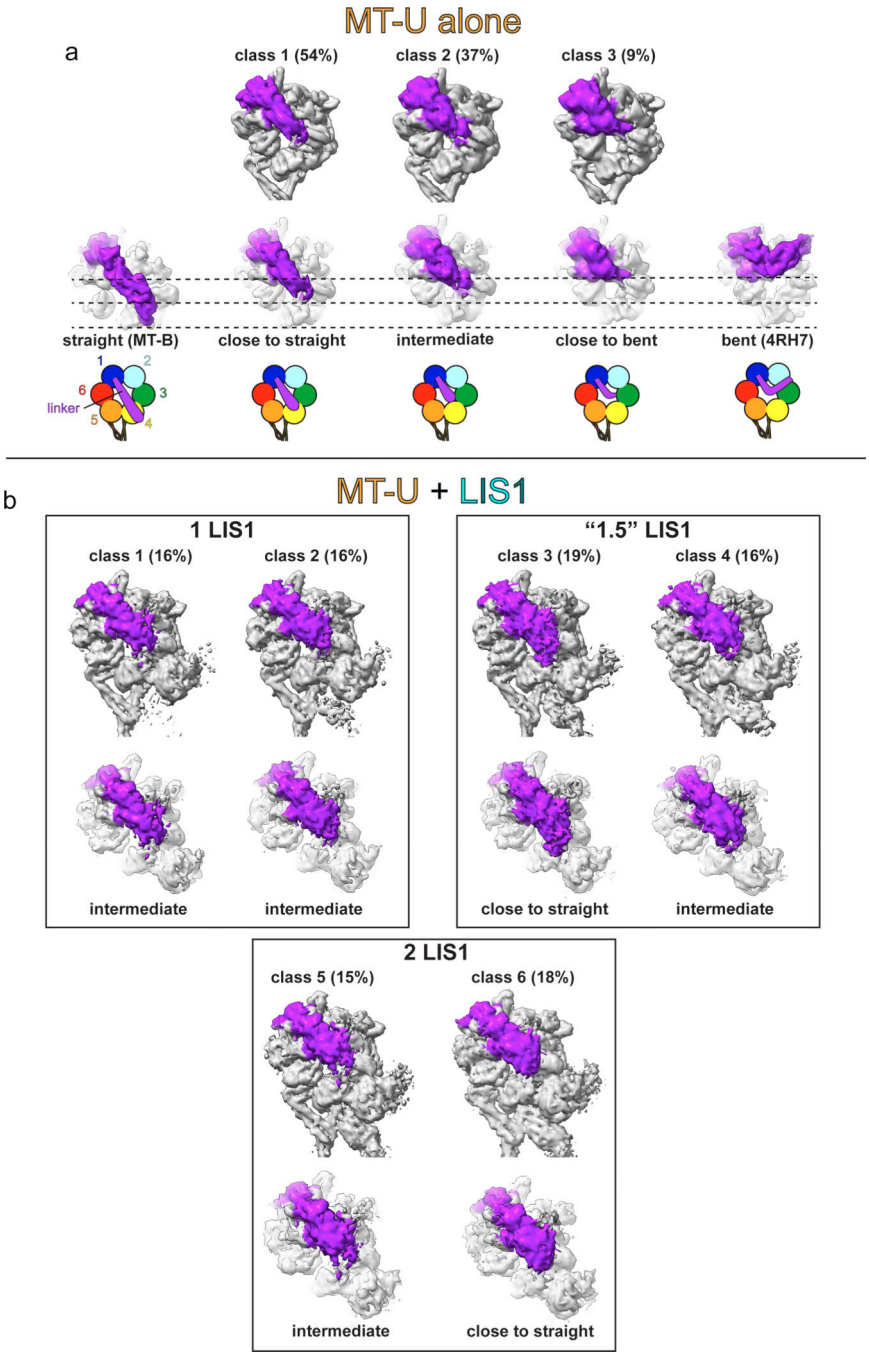

Extended Data Figure 10. 3D classification reveals flexibility of MT-U linker that is independent of LIS1 binding.

(A) 3D classification results for MT-U alone. Front views of the motor, and zoomed-in views of the linker (colored in purple) are shown. The linker position is indicated in the cartoon model. The map contour levels are all set to 0.45. Note that no obvious bent linker was observed in any class. (B) 3D classification results of MT-U with LIS1. The classification

is mainly guided by LIS1 occupancy, but the linker flexibility can also be visualized at low map contour levels (all set to 0.2). For all classes, the linker position is flexible. No obvious bent linker was observed regardless of LIS1 occupancy.

Supplementary Material

Refer to Web version on PubMed Central for supplementary material.

ACKNOWLEDGEMENTS

We are very grateful to Janelia Research Campus for providing fluorescent Halo and SNAP dyes, Andrew Carter and Sami Chabaan for valuable discussions (and for sharing data that was unpublished at the time), and to members of the Markus and DeLuca laboratories for valuable discussions. This work was funded by the NIH/NIGMS (R35GM139483 to S.M.M., and R35GM142959 to K.Z.). The funders had no role in study design, data collection and analysis, decision to publish or preparation of this manuscript. We would like to thank Kaifeng Zhou, Jianfeng Lin for the help with cryo-EM data collection at Yale ScienceHill-Cryo-EM facility. The Yale Cryo-EM Resource is funded in part by the NIH grant S10OD023603. We thank Liguo Wang, Jake Kaminsky, Guobin Hu at the Laboratory for BioMolecular Structure (LBMS) for help on cryo-EM data collection. The LBMS is supported by the DOE Office of Biological and Environmental Research (KP1607011).

DATA AVAILABILITY

Models and cryo-EM maps have been deposited in the PDB and EMDB as follows: 8FCY/EMD-28999 ($dynein_{MOTOR}^{MT\text{-}B}$ in ATP), 8FD6/EMD-29003 ($dynein_{MOTOR}^{MT\text{-}U}$ in ATP and Vi), 8FDT/EMD-29012 ($dynein_{MOTOR}^{MT\text{-}U}$ + LIS1 in ATP and Vi), and 8FDU/EMD-29014 ($dynein_{MOTOR}^{MT\text{-}U}$ + LIS1 in ATP and Vi, locally refined at AAA3-AAA5 and 2 LIS1s). Note the residues labeled in the figures for human dynein are based on the Cytoplasmic Dynein-1 Heavy Chain 1 sequence (Q14204). All of the plasmids, yeast strains, datasets and raw video files that were generated during and/or analyzed during this study are available from the corresponding authors upon request. All data used to generate plots throughout the manuscript are included as Source Data files, as are raw images of uncropped gels. PDB models used throughout this study include 5NUG[3], 4RH7[37], 7MGM[39], 8DYU[41], 7ZG8[38], 3VKG[80], 4AKG[81], 4W8F[82], and 1UUJ[83].

REFERENCES

1. Canty JT, Tan R, Kusakci E, Fernandes J. & Yildiz A. Structure and Mechanics of Dynein Motors. Annu Rev Biophys 50, 549–574, (2021). [PubMed: 33957056]
2. Marzo MG, Griswold JM & Markus SM Pac1/LIS1 stabilizes an uninhibited conformation of dynein to coordinate its localization and activity. Nat Cell Biol 22, 559–569, (2020). [PubMed: 32341548]
3. Zhang K, Foster HE, Rondelet A, Lacey SE, Bahi-Buisson N, Bird AW & Carter AP Cryo-EM Reveals How Human Cytoplasmic Dynein Is Auto-inhibited and Activated. Cell 169, 1303–1314 e1318, (2017). [PubMed: 28602352]
4. Amos LA Brain dynein crossbridges microtubules into bundles. J Cell Sci 93 (Pt 1), 19–28, (1989). [PubMed: 2533206]
5. McKenney RJ, Huynh W, Tanenbaum ME, Bhabha G. & Vale RD Activation of cytoplasmic dynein motility by dynactin-cargo adapter complexes. Science 345, 337–341, (2014). [PubMed: 25035494]
6. Schlager MA, Hoang HT, Urnavicius L, Bullock SL & Carter AP In vitro reconstitution of a highly processive recombinant human dynein complex. EMBO J 33, 1855–1868, (2014). [PubMed: 24986880]

7. Markus SM, Marzo MG & McKenney RJ New insights into the mechanism of dynein motor regulation by lissencephaly-1. eLife 9, (2020).
8. Reiner O, Carrozzo R, Shen Y, Wehnert M, Faustinella F, Dobyns WB, Caskey CT & Ledbetter DH Isolation of a Miller-Dieker lissencephaly gene containing G protein beta-subunit-like repeats. Nature 364, 717–721, (1993). [PubMed: 8355785]
9. Qiu R, Zhang J. & Xiang X. LIS1 regulates cargo-adapter-mediated activation of dynein by overcoming its autoinhibition in vivo. J Cell Biol 218, 3630–3646, (2019). [PubMed: 31562232]
10. Htet ZM, Gillies JP, Baker RW, Leschziner AE, DeSantis ME & Reck-Peterson SL LIS1 promotes the formation of activated cytoplasmic dynein-1 complexes. Nat Cell Biol, (2020).
11. Elshenawy MM, Kusakci E, Volz S, Baumbach J, Bullock SL & Yildiz A. Lis1 activates dynein motility by modulating its pairing with dynactin. Nat Cell Biol, (2020).
12. Lee WL, Oberle JR & Cooper JA The role of the lissencephaly protein Pac1 during nuclear migration in budding yeast. J Cell Biol 160, 355–364, (2003). [PubMed: 12566428]
13. Coquelle FM, Caspi M, Cordelieres FP, Dompierre JP, Dujardin DL, Koifman C, Martin P, Hoogenraad CC, Akhmanova A, Galjart N, De Mey JR & Reiner O. LIS1, CLIP-170's key to the dynein/dynactin pathway. Mol Cell Biol 22, 3089–3102, (2002). [PubMed: 11940666]
14. Faulkner NE, Dujardin DL, Tai CY, Vaughan KT, O'Connell CB, Wang Y. & Vallee RB A role for the lissencephaly gene LIS1 in mitosis and cytoplasmic dynein function. Nat Cell Biol 2, 784–791, (2000). [PubMed: 11056532]
15. Moon HM, Youn YH, Pemble H, Yingling J, Wittmann T. & Wynshaw-Boris A. LIS1 controls mitosis and mitotic spindle organization via the LIS1-NDEL1-dynein complex. Hum Mol Genet 23, 449–466, (2014). [PubMed: 24030547]
16. Splinter D, Razafsky DS, Schlager MA, Serra-Marques A, Grigoriev I, Demmers J, Keijzer N, Jiang K, Poser I, Hyman AA, Hoogenraad CC, King SJ & Akhmanova A. BICD2, dynactin, and LIS1 cooperate in regulating dynein recruitment to cellular structures. Mol Biol Cell 23, 4226–4241, (2012). [PubMed: 22956769]
17. Sheeman B, Carvalho P, Sagot I, Geiser J, Kho D, Hoyt MA & Pellman D. Determinants of S. cerevisiae dynein localization and activation: implications for the mechanism of spindle positioning. Curr Biol 13, 364–372, (2003). [PubMed: 12620184]
18. Baumbach J, Murthy A, McClintock MA, Dix CI, Zalyte R, Hoang HT & Bullock SL Lissencephaly-1 is a context-dependent regulator of the human dynein complex. eLife 6, (2017).
19. Gutierrez PA, Ackermann BE, Vershinin M. & McKenney RJ Differential effects of the dynein-regulatory factor Lissencephaly-1 on processive dynein-dynactin motility. J Biol Chem 292, 12245–12255, (2017). [PubMed: 28576829]
20. Jha R, Roostalu J, Cade NI, Trokter M. & Surrey T. Combinatorial regulation of the balance between dynein microtubule end accumulation and initiation of directed motility. EMBO J 36, 3387–3404, (2017). [PubMed: 29038173]
21. Lammers LG & Markus SM The dynein cortical anchor Num1 activates dynein motility by relieving Pac1/LIS1-mediated inhibition. J Cell Biol 211, 309–322, (2015). [PubMed: 26483554]
22. Lenz JH, Schuchardt I, Straube A. & Steinberg G. A dynein loading zone for retrograde endosome motility at microtubule plus-ends. EMBO J 25, 2275–2286, (2006). [PubMed: 16688221]
23. Egan MJ, Tan K. & Reck-Peterson SL Lis1 is an initiation factor for dynein-driven organelle transport. J Cell Biol 197, 971–982, (2012). [PubMed: 22711696]
24. Markus SM & Lee WL Regulated offloading of cytoplasmic dynein from microtubule plus ends to the cortex. Dev Cell 20, 639–651, (2011). [PubMed: 21571221]
25. Markus SM, Plevock KM, St Germain BJ, Punch JJ, Meaden CW & Lee WL Quantitative analysis of Pac1/LIS1-mediated dynein targeting: Implications for regulation of dynein activity in budding yeast. Cytoskeleton (Hoboken) 68, 157–174, (2011). [PubMed: 21294277]
26. Hu CD, Chinenov Y. & Kerppola TK Visualization of interactions among bZIP and Rel family proteins in living cells using bimolecular fluorescence complementation. Mol Cell 9, 789–798, (2002). [PubMed: 11983170]
27. Toropova K, Zou S, Roberts AJ, Redwine WB, Goodman BS, Reck-Peterson SL & Leschziner AE Lis1 regulates dynein by sterically blocking its mechanochemical cycle. eLife 3, (2014).

28. Huang J, Roberts AJ, Leschziner AE & Reck-Peterson SL Lis1 acts as a "clutch" between the ATPase and microtubule-binding domains of the dynein motor. Cell 150, 975–986, (2012). [PubMed: 22939623]
29. McKenney RJ, Vershinin M, Kunwar A, Vallee RB & Gross SP LIS1 and NudE induce a persistent dynein force-producing state. Cell 141, 304–314, (2010). [PubMed: 20403325]
30. Lacey SE, He S, Scheres SH & Carter AP Cryo-EM of dynein microtubule-binding domains shows how an axonemal dynein distorts the microtubule. eLife 8, (2019).
31. Nishida N, Komori Y, Takarada O, Watanabe A, Tamura S, Kubo S, Shimada I. & Kikkawa M. Structural basis for two-way communication between dynein and microtubules. Nature communications 11, 1038, (2020).
32. Carter AP, Garbarino JE, Wilson-Kubalek EM, Shipley WE, Cho C, Milligan RA, Vale RD & Gibbons IR Structure and functional role of dynein's microtubule-binding domain. Science 322, 1691–1695, (2008). [PubMed: 19074350]
33. Gibbons IR, Garbarino JE, Tan CE, Reck-Peterson SL, Vale RD & Carter AP The affinity of the dynein microtubule-binding domain is modulated by the conformation of its coiled-coil stalk. J Biol Chem 280, 23960–23965, (2005). [PubMed: 15826937]
34. Kon T, Imamula K, Roberts AJ, Ohkura R, Knight PJ, Gibbons IR, Burgess SA & Sutoh K. Helix sliding in the stalk coiled coil of dynein couples ATPase and microtubule binding. Nat Struct Mol Biol 16, 325–333, (2009). [PubMed: 19198589]
35. Markus SM, Punch JJ & Lee WL Motor- and tail-dependent targeting of dynein to microtubule plus ends and the cell cortex. Curr Biol 19, 196–205, (2009). [PubMed: 19185494]
36. Young G, Hundt N, Cole D, Fineberg A, Andrecka J, Tyler A, Olerinyova A, Ansari A, Marklund EG, Collier MP, Chandler SA, Tkachenko O, Allen J, Crispin M, Billington N, Takagi Y, Sellers JR, Eichmann C, Selenko P, Frey L, Riek R, Galpin MR, Struwe WB, Benesch JLP & Kukura P. Quantitative mass imaging of single biological macromolecules. Science 360, 423–427, (2018). [PubMed: 29700264]
37. Schmidt H, Zalyte R, Urnavicius L. & Carter AP Structure of human cytoplasmic dynein-2 primed for its power stroke. Nature 518, 435–438, (2015). [PubMed: 25470043]
38. Chaaban S. & Carter AP Structure of dynein-dynactin on microtubules shows tandem adaptor binding. Nature 610, 212–216, (2022). [PubMed: 36071160]
39. Gillies JP, Reimer JM, Karasmanis EP, Lahiri I, Htet ZM, Leschziner AE & Reck-Peterson SL Structural basis for cytoplasmic dynein-1 regulation by Lis1. eLife 11, (2022).
40. DeSantis ME, Cianfrocco MA, Htet ZM, Tran PT, Reck-Peterson SL & Leschziner AE Lis1 Has Two Opposing Modes of Regulating Cytoplasmic Dynein. Cell 170, 1197–1208 e1112, (2017). [PubMed: 28886386]
41. Reimer JM, DeSantis ME, Reck-Peterson SL & Leschziner AE Structures of human dynein in complex with the lissencephaly 1 protein, LIS1. eLife 12, (2023).
42. Torres FR, Montenegro MA, Marques-De-Faria AP, Guerreiro MM, Cendes F. & Lopes-Cendes I. Mutation screening in a cohort of patients with lissencephaly and subcortical band heterotopia. Neurology 62, 799–802, (2004). [PubMed: 15007136]
43. Tate JG, Bamford S, Jubb HC, Sondka Z, Beare DM, Bindal N, Boutselakis H, Cole CG, Creatore C, Dawson E, Fish P, Harsha B, Hathaway C, Jupe SC, Kok CY, Noble K, Ponting L, Ramshaw CC, Rye CE, Speedy HE, Stefancsik R, Thompson SL, Wang S, Ward S, Campbell PJ & Forbes SA COSMIC: the Catalogue Of Somatic Mutations In Cancer. Nucleic Acids Res 47, D941–D947, (2019). [PubMed: 30371878]
44. Burgess SA, Walker ML, Sakakibara H, Knight PJ & Oiwa K. Dynein structure and power stroke. Nature 421, 715–718, (2003). [PubMed: 12610617]
45. Kon T, Nishiura M, Ohkura R, Toyoshima YY & Sutoh K. Distinct functions of nucleotide-binding/hydrolysis sites in the four AAA modules of cytoplasmic dynein. Biochemistry 43, 11266–11274, (2004). [PubMed: 15366936]
46. Imamula K, Kon T, Ohkura R. & Sutoh K. The coordination of cyclic microtubule association/dissociation and tail swing of cytoplasmic dynein. Proc Natl Acad Sci U S A 104, 16134–16139, (2007). [PubMed: 17911268]

47. Uchimura S, Fujii T, Takazaki H, Ayukawa R, Nishikawa Y, Minoura I, Hachikubo Y, Kurisu G, Sutoh K, Kon T, Namba K. & Muto E. A flipped ion pair at the dynein-microtubule interface is critical for dynein motility and ATPase activation. J Cell Biol 208, 211–222, (2015). [PubMed: 25583999]

48. Duellberg C, Trokter M, Jha R, Sen I, Steinmetz MO & Surrey T. Reconstitution of a hierarchical +TIP interaction network controlling microtubule end tracking of dynein. Nat Cell Biol, (2014).

49. Cardoso C, Leventer RJ, Matsumoto N, Kuc JA, Ramocki MB, Mewborn SK, Dudlicek LL, May LF, Mills PL, Das S, Pilz DT, Dobyns WB & Ledbetter DH The location and type of mutation predict malformation severity in isolated lissencephaly caused by abnormalities within the LIS1 gene. Hum Mol Genet 9, 3019–3028, (2000). [PubMed: 11115846]

50. Pilz DT, Matsumoto N, Minnerath S, Mills P, Gleeson JG, Allen KM, Walsh CA, Barkovich AJ, Dobyns WB, Ledbetter DH & Ross ME LIS1 and XLIS (DCX) mutations cause most classical lissencephaly, but different patterns of malformation. Hum Mol Genet 7, 2029–2037, (1998). [PubMed: 9817918]

51. Sapir T, Eisenstein M, Burgess HA, Horesh D, Cahana A, Aoki J, Hattori M, Arai H, Inoue K. & Reiner O. Analysis of lissencephaly-causing LIS1 mutations. Eur J Biochem 266, 1011–1020, (1999). [PubMed: 10583396]

52. Karasmanis EP, Reimer JM, Kendrick AA, Rodriguez JA, Truong JB, Lahiri I, Reck-Peterson SL & Leschziner AE Lis1 relieves cytoplasmic dynein-1 auto-inhibition by acting as a molecular wedge. bioRxiv, 2022.2010.2010.511666, (2022).

METHODS ONLY REFERENCES

53. Bi E. & Pringle JR ZDS1 and ZDS2, genes whose products may regulate Cdc42p in Saccharomyces cerevisiae. Mol Cell Biol 16, 5264–5275, (1996). [PubMed: 8816439]

54. Knop M, Siegers K, Pereira G, Zachariae W, Winsor B, Nasmyth K. & Schiebel E. Epitope tagging of yeast genes using a PCR-based strategy: more tags and improved practical routines. Yeast 15, 963–972, (1999). [PubMed: 10407276]

55. Longtine MS, McKenzie A 3rd, Demarini DJ, Shah NG, Wach A, Brachat A, Philippsen P. & Pringle JR Additional modules for versatile and economical PCR-based gene deletion and modification in Saccharomyces cerevisiae. Yeast 14, 953–961, (1998). [PubMed: 9717241]

56. Markus SM, Omer S, Baranowski K. & Lee WL Improved Plasmids for Fluorescent Protein Tagging of Microtubules in Saccharomyces cerevisiae. Traffic 16, 773–786, (2015). [PubMed: 25711127]

57. Gibson DG, Young L, Chuang RY, Venter JC, Hutchison CA 3rd & Smith HO Enzymatic assembly of DNA molecules up to several hundred kilobases. Nat Methods 6, 343–345, (2009). [PubMed: 19363495]

58. Marzo MG, Griswold JM, Ruff KM, Buchmeier RE, Fees CP & Markus SM Molecular basis for dyneinopathies reveals insight into dynein regulation and dysfunction. eLife 8, (2019).

59. Ecklund KH, Morisaki T, Lammers LG, Marzo MG, Stasevich TJ & Markus SM She1 affects dynein through direct interactions with the microtubule and the dynein microtubule-binding domain. Nature communications 8, 2151, (2017).

60. Cheng K, Wilkinson M, Chaban Y. & Wigley DB A conformational switch in response to Chi converts RecBCD from phage destruction to DNA repair. Nat Struct Mol Biol 27, 71–77, (2020). [PubMed: 31907455]

61. Mastronarde DN Automated electron microscope tomography using robust prediction of specimen movements. J Struct Biol 152, 36–51, (2005). [PubMed: 16182563]

62. Punjani A, Rubinstein JL, Fleet DJ & Brubaker MA cryoSPARC: algorithms for rapid unsupervised cryo-EM structure determination. Nat Methods 14, 290–296, (2017). [PubMed: 28165473]

63. Bepler T, Morin A, Rapp M, Brasch J, Shapiro L, Noble AJ & Berger B. Positive-unlabeled convolutional neural networks for particle picking in cryo-electron micrographs. Nat Methods 16, 1153–1160, (2019). [PubMed: 31591578]

64. Punjani A, Zhang H. & Fleet DJ Non-uniform refinement: adaptive regularization improves single-particle cryo-EM reconstruction. Nat Methods 17, 1214–1221, (2020). [PubMed: 33257830]

65. Tan YZ, Baldwin PR, Davis JH, Williamson JR, Potter CS, Carragher B. & Lyumkis D. Addressing preferred specimen orientation in single-particle cryo-EM through tilting. Nat Methods 14, 793–796, (2017). [PubMed: 28671674]

66. Goddard TD, Huang CC, Meng EC, Pettersen EF, Couch GS, Morris JH & Ferrin TE UCSF ChimeraX: Meeting modern challenges in visualization and analysis. Protein Sci 27, 14–25, (2018). [PubMed: 28710774]

67. Kidmose RT, Juhl J, Nissen P, Boesen T, Karlsen JL & Pedersen BP Namdinator - automatic molecular dynamics flexible fitting of structural models into cryo-EM and crystallography experimental maps. IUCrJ 6, 526–531, (2019).

68. Casanal A, Lohkamp B. & Emsley P. Current developments in Coot for macromolecular model building of Electron Cryo-microscopy and Crystallographic Data. Protein Sci 29, 1069–1078, (2020). [PubMed: 31730249]

69. Brown A, Long F, Nicholls RA, Toots J, Emsley P. & Murshudov G. Tools for macromolecular model building and refinement into electron cryo-microscopy reconstructions. Acta Crystallogr D Biol Crystallogr 71, 136–153, (2015). [PubMed: 25615868]

70. Jumper J, Evans R, Pritzel A, Green T, Figurnov M, Ronneberger O, Tunyasuvunakool K, Bates R, Zidek A, Potapenko A, Bridgland A, Meyer C, Kohl SAA, Ballard AJ, Cowie A, Romera-Paredes B, Nikolov S, Jain R, Adler J, Back T, Petersen S, Reiman D, Clancy E, Zielinski M, Steinegger M, Pacholska M, Berghammer T, Bodenstein S, Silver D, Vinyals O, Senior AW, Kavukcuoglu K, Kohli P. & Hassabis D. Highly accurate protein structure prediction with AlphaFold. Nature 596, 583–589, (2021). [PubMed: 34265844]

71. Afonine PV, Poon BK, Read RJ, Sobolev OV, Terwilliger TC, Urzhumtsev A. & Adams PD Real-space refinement in PHENIX for cryo-EM and crystallography. Acta Crystallogr D Struct Biol 74, 531–544, (2018). [PubMed: 29872004]

72. Chen VB, Arendall WB 3rd, Headd JJ, Keedy DA, Immormino RM, Kapral GJ, Murray LW, Richardson JS & Richardson DC MolProbity: all-atom structure validation for macromolecular crystallography. Acta Crystallogr D Biol Crystallogr 66, 12–21, (2010). [PubMed: 20057044]

73. Jo S, Kim T, Iyer VG & Im W. CHARMM-GUI: a web-based graphical user interface for CHARMM. J Comput Chem 29, 1859–1865, (2008). [PubMed: 18351591]

74. Thompson A, Aktulga HM, Berger R, Bolintineanu DS, Brown WM, Crozier PS, in t' Veld PJ, Kohlmeyer A, Moore SG, Nguyen TD, Shan R, Stevens MJ, Tranchida J, Trott C. & Plimpton SJ LAMMPS - a flexible simulation tool for particle-based materials modeling at the atomic, meso, and continuum scales. Computer Physics Communications 271, (2022).

75. Berendsen H, Van Gunsteren W, Egberts E. & De Vlieg J. Dynamic simulation of complex molecular systems. Supercomputer Research in Chemistry and Chemical Engineering 353, 106–122, (1987).

76. Ryckaert J-P, Ciccotti G. & Berendsen H. Numerical integration of the Cartesian Equations of Motion of a System with Constraints: Molecular Dynamics of n-Alkanes. J. Of Computational Physics 23, 327–341, (1977).

77. Jones JE & Ingham AE On the calculation of certain crystal potential constants, and on the cubic crystal of least potential energy. Proceedings of the Royal Society of London Series A, Containing Papers of a Mathematical and Physical Character 636–653, (1925).

78. Hockney RW & Eastwood JW Computer Simulation Using Particles. CRC Press, (1988).

79. Evans DJ & Holian BL The nose–hoover thermostat. The Journal of chemical physics 83, 4069–4074, (1985).

80. Kon T, Oyama T, Shimo-Kon R, Imamula K, Shima T, Sutoh K. & Kurisu G. The 2.8 A crystal structure of the dynein motor domain. Nature 484, 345–350, (2012). [PubMed: 22398446]

81. Schmidt H, Gleave ES & Carter AP Insights into dynein motor domain function from a 3.3-A crystal structure. Nat Struct Mol Biol 19, 492–497, S491, (2012). [PubMed: 22426545]

82. Bhabha G, Cheng HC, Zhang N, Moeller A, Liao M, Speir JA, Cheng Y. & Vale RD Allosteric communication in the Dynein motor domain. Cell 159, 857–868, (2014). [PubMed: 25417161]

83. Kim MH, Cooper DR, Oleksy A, Devedjiev Y, Derewenda U, Reiner O, Otlewski J. & Derewenda ZS The structure of the N-terminal domain of the product of the lissencephaly gene Lis1 and its functional implications. Structure 12, 987–998, (2004). [PubMed: 15274919]

84. Karasmanis EP, Reimer JM, Kendrick AA, Rodriguez JA, Truong JB, Lahiri I, Reck-Peterson SL & Leschziner AE Lis1 relieves cytoplasmic dynein-1 auto-inhibition by acting as a molecular wedge. bioRxiv, 2022.2010.2010.511666, (2022).

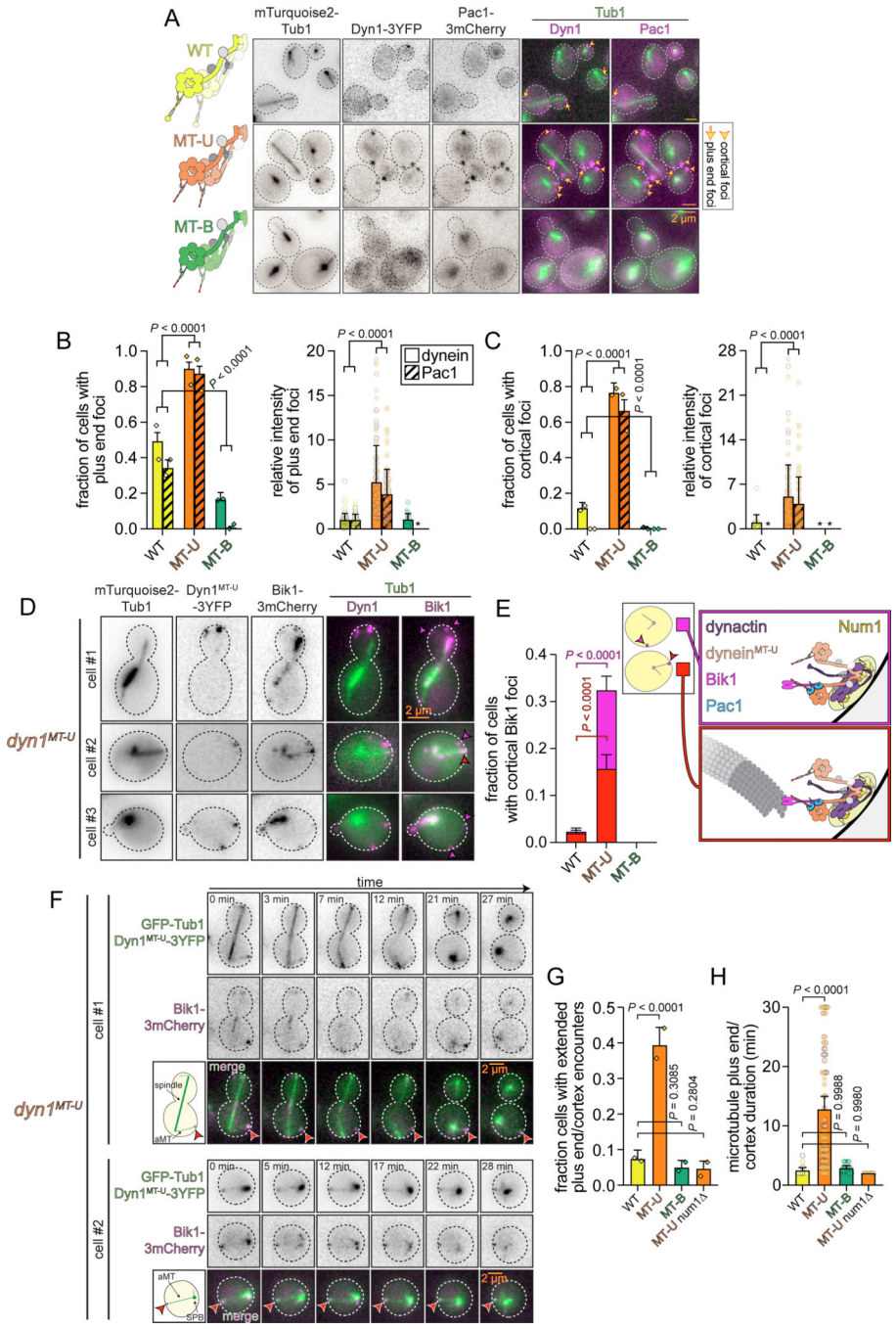

Figure 1. The microtubule-unbound dynein mutant is tightly bound to Pac1, Bik1, and microtubule plus ends in cells.

(A) Representative images of cells expressing Pac1–3mCherry, mTurquoise2-Tub1, and either Dyn1^{MT-U}-3YFP or Dyn1^{MT-B}-3YFP. (B and C) Plots (mean ± SD, along with all data points) depicting frequency and relative intensity of plus end (B) and cortical (C) dynein and Pac1 foci in cells expressing indicated *DYN1* allele as the only source of dynein heavy chain (WT, wild-type; MT-U, microtubule-unbound mutant; MT-B, microtubule-bound mutant; *, no foci observed; n = 101/25 plus end/cortical dynein foci, and 73/0 plus end/cortical Pac1 foci from 213 *DYN1* cells; 114/108 plus end/cortical dynein foci, and 116/87 plus

end/cortical Pac1 foci from 110 *dyn1*$^{MT-U}$ cells; 24/0 plus end/cortical dynein foci, and 1/0 plus end/cortical Pac1 foci from 147 *dyn1*$^{MT-B}$ cells; all from 2 biological replicates). (D) Representative images of cells expressing Bik1–3mCherry, mTurquoise2-Tub1, and Dyn1^{MT-U}-3YFP (magenta arrowhead, cortical Bik1 foci without associated plus end; red arrowhead, cortical Bik1 focus with associated plus end). (E) Plot (mean ± SD) depicting frequency of cells with indicated dynein allele possessing cortical Bik1 foci (either with or without associated microtubule plus end, as indicated; n = 305, 281, and 226 *DYN1*, *dyn1*$^{MT-U}$, and *dyn1*$^{MT-B}$ cells, respectively, from 2 independent replicates). (F) Representative timelapse images of cells expressing Bik1–3mCherry, GFP-Tub1, and Dyn1^{MT-U}-3YFP (arrowheads, instances of plus ends with Bik1 foci statically associated with the cortex for 27–28 minutes). Cartoons represent cell in first frame of movie (aMT, astral microtubule; SPB, spindle pole body; magenta circles, plus end Bik1 foci statically associated with cortex). Also see Video S1. (G and H) Plots (mean ± SD, along with all data points) depicting frequency (G) and duration (H) of extended plus end-cortex encounters (those lasting ≥ 2 minutes) in cells with indicated dynein and/or Num1 allele (n = 15 events from 206 DYN1 cells, 74 events from 188 *dyn1*$^{MT-U}$ cells, 12 events from 241 *dyn1*$^{MT-B}$ cells, and 8 events from 173 *dyn1*$^{MT-U}$ *num1Δ* cells, all from 2 independent replicates; note that cells used in panels F-H are distinct biological isolates of those used in panels D and E). Two-tailed *P* values were calculated from Z scores for proportion data, or by comparing means using a Dunnett's test (for intensity values and microtubule-cortex duration values).

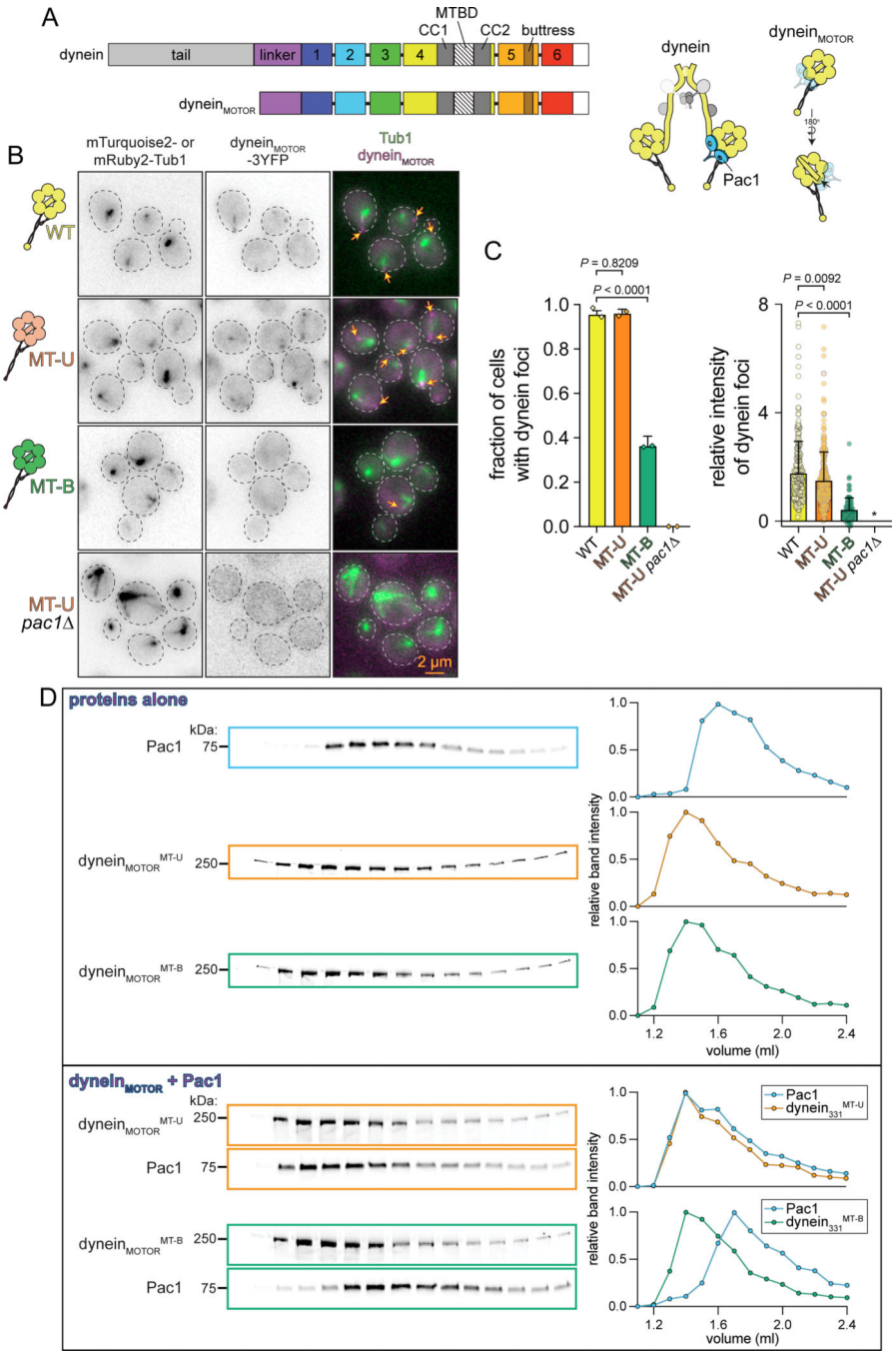

Figure 2. The dynein motor domain is sufficient for microtubule-binding-induced allostery.

(A) Schematic and cartoon depictions of full-length and the truncated dynein motor domain used here (CC, coiled-coil; MTBD, microtubule-binding domain). Arrow on cartoon indicates truncated dynein linker that does not contact Pac1[27]. Note the truncated motor domain lacks the tail domain, which is required for Num1 and dynactin binding[35]. (B) Representative fluorescence images of cells expressing mTurquoise2- (for all strains except $dyn1_{MOTOR}^{MT\text{-}U}$ *pac1Δ*) or mRuby2-Tub1 and indicated dynein motor domain fragment (arrows, plus end foci). (C) Plots (mean ± SD, with means from each replicate indicated

by diamonds on fraction plots, or different shade circles for all data points on intensity plots) depicting frequency and relative intensity of dynein foci, which were scored from timelapse movies (n = 278 foci from 196 wild-type $dyn1_{MOTOR}$ cells; 240 foci from 194 $dyn1_{MOTOR}^{MT\text{-}U}$ cells; 97 foci from 224 $dyn1_{MOTOR}^{MT\text{-}B}$ cells; 0 foci from 251 $dyn1_{MOTOR}^{MT\text{-}U}$ *pac1Δ* cells; all from 2 biological replicates). All intensity values were normalized to the mean values (for each replicate) for $dynein_{MOTOR}$-3YFP in wild-type cells (set to 1). Two-tailed *P* values were calculated from Z scores (for proportion data) or by comparing means using a Dunnett's test (for intensity values). (D) Analytical size exclusion chromatography analysis showing proteins alone (top), or mixed prior to running on a Superdex 5/150 (bottom). Plots depict band intensity profiles. Gels and accompanying analyses are representative of at least 3 independent replicates.

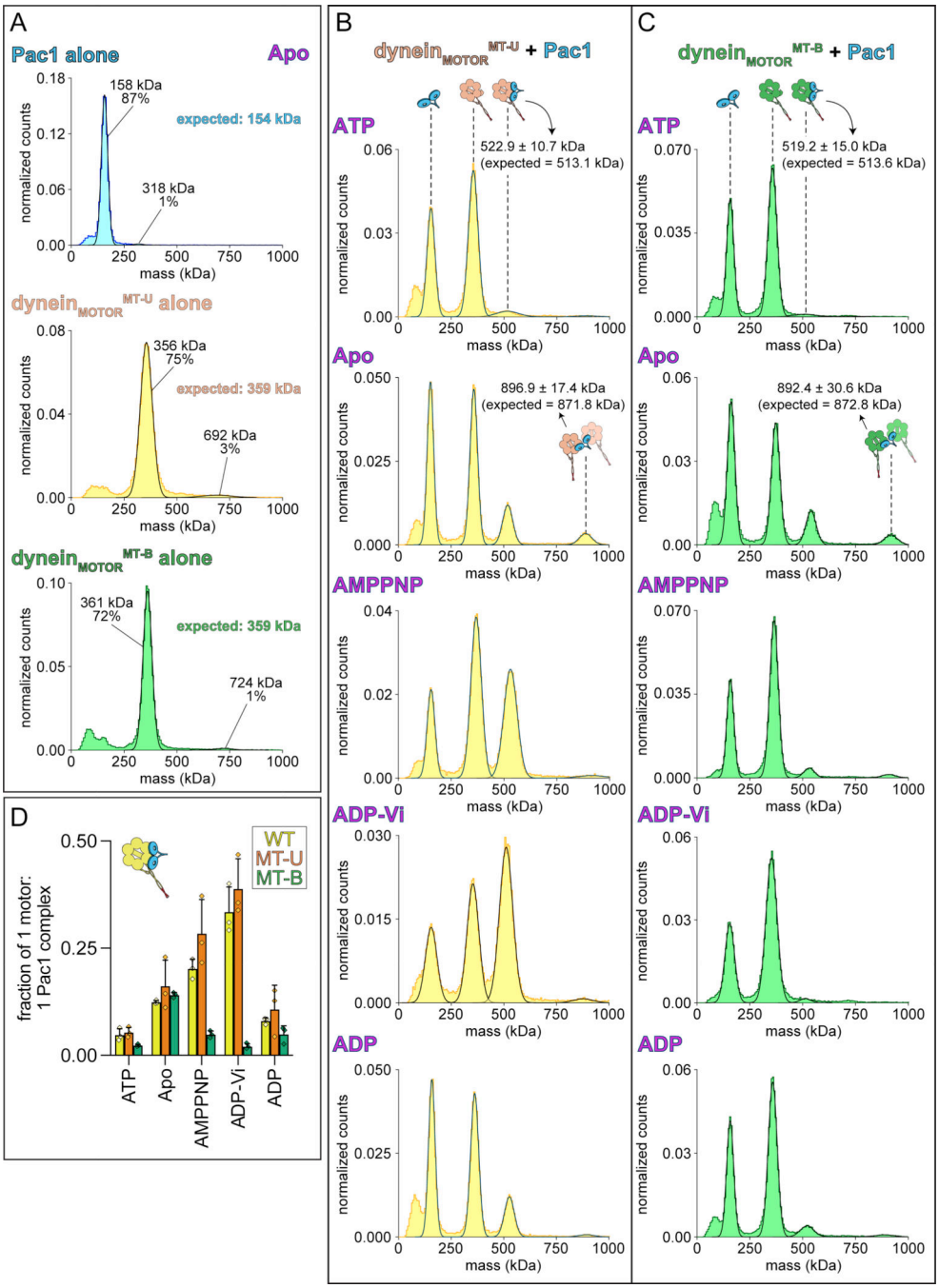

Figure 3. Mass photometric analysis of Pac1-dynein$_{MOTOR}$ binding.

(A) Proteins purified from yeast were diluted into assay buffer without nucleotide, and movies were acquired on a Refeyn TwoMP immediately thereafter. The masses of protein species landing on the glass coverslip were empirically determined by converting particle contrast to mass following a calibration routine in the Refeyn software. Fitting of raw data, which identifies mean mass values for each species, and relative fraction of particles with indicated mass, was performed in Discover MP. Note the majority of Pac1 exists as a dimer, while the motor domains are largely monomeric. (B and C) Histograms depicting

relative fraction of Pac1 alone, dynein$_{MOTOR}$ alone (MT-U or MT-B), or dynein$_{MOTOR}$-Pac1 complex. Equimolar concentrations of Pac1 and either dynein$_{MOTOR}^{MT\text{-}U}$ (B) or dynein$_{MOTOR}^{MT\text{-}B}$ (C; 25 nM each) were mixed in assay buffer with indicated nucleotide (1 mM), incubated for 1–2 minutes, and then diluted to 5 nM on a coverslip mounted on a Refeyn TwoMP. Movies were acquired immediately thereafter, and mass analysis was performed using Discover MP. Note those particles within the 523 kDa peak correspond to 1 Pac1 dimer:1 dynein$_{MOTOR}$ monomer complexes, while those within the 897 kDa peak likely correspond to 1 Pac1 dimer:2 dynein$_{MOTOR}$ complexes (see cartoon schematic above each peak). Plots depict representative data of at least 3 independent replicates for each. (D) The relative fraction of 1 Pac1 dimer:1 dynein$_{MOTOR}$ monomer complexes are plotted (mean ± SD, along with all data points). See Extended Data Figure 2B for representative mass histograms with the wild-type dynein$_{MOTOR}$ protein with and without Pac1 (n = 3 independent replicate for each). Note that we observed an apparently smaller fraction of dynein-Pac1 complex formation by mass photometry compared to our analytical gel filtration data (Figure 2D). This is likely a consequence of the lower concentrations needed for mass photometry (~20-fold difference; see Methods).

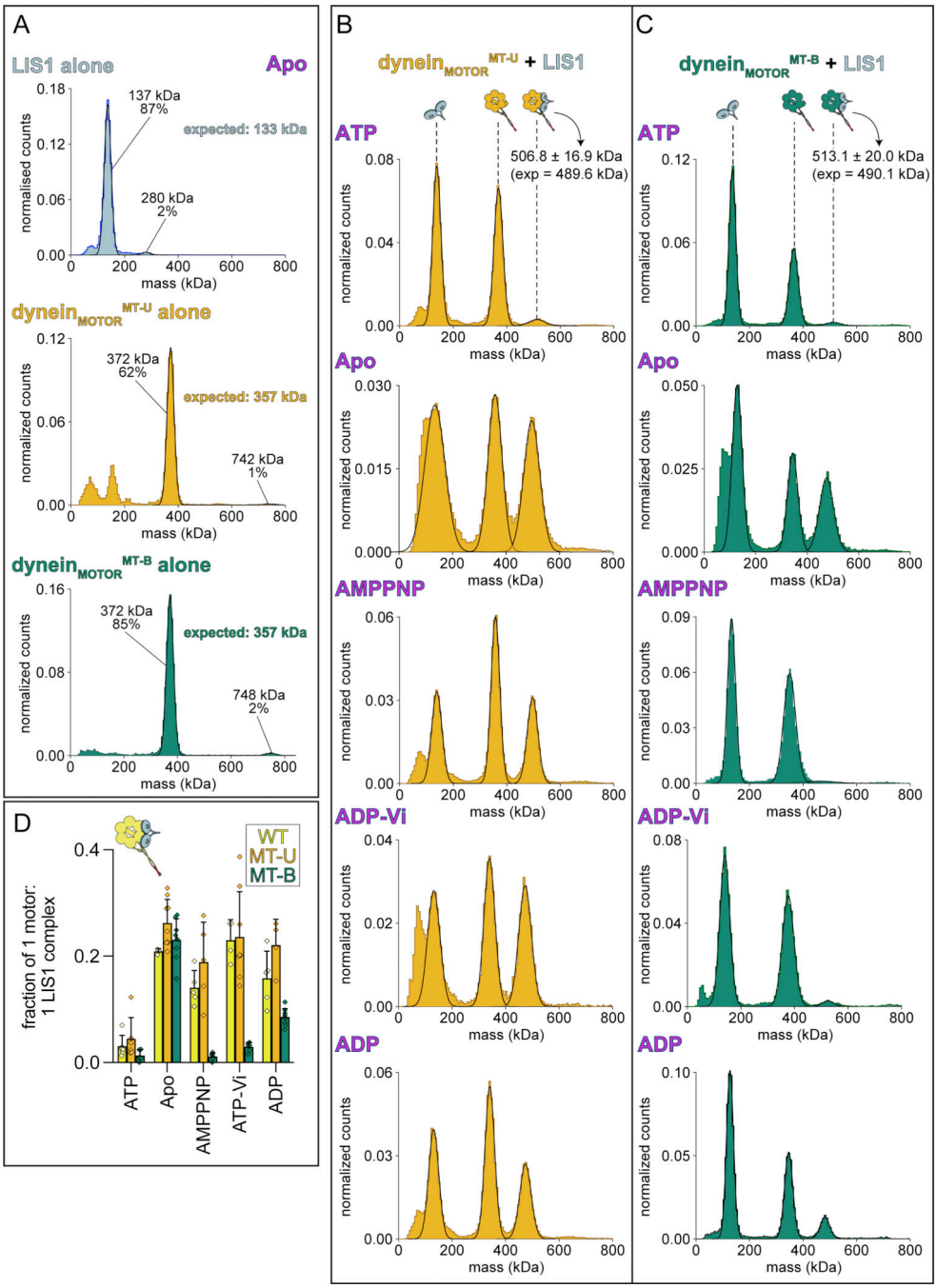

Figure 4. Mass photometric analysis of human LIS1-dynein$_{MOTOR}$ binding.

(A) Proteins purified from insect cells were diluted into assay buffer without nucleotide, and movies were acquired on a Refeyn TwoMP immediately thereafter, as described in Figure 3. Note the majority of LIS1 exists as a dimer, while the motor domains are largely monomeric. (B and C) LIS1 and either human dynein$_{MOTOR}^{MT-U}$ (B) or dynein$_{MOTOR}^{MT-B}$ (C) were mixed in assay buffer with indicated nucleotide (to 25 nM each), incubated for 1–2 minutes, and then diluted to 5 nM on the Refeyn TwoMP. Movies were acquired immediately thereafter, and mass analysis was performed using Discover MP. Note those

particles within the 507 kDa peak correspond to 1 LIS1 dimer:1 dynein$_{MOTOR}$ monomer complexes (see cartoon schematic above each peak). We did not observe protein species that would correspond to the 1 LIS1 dimer:2 dynein$_{MOTOR}$ complexes observed with yeast proteins in Figure 3. Plots depict representative data of at least 3 independent replicates for each. (D) The relative fraction of 1 LIS1 dimer:1 dynein$_{MOTOR}$ monomer complexes are plotted (mean ± SD, along with all data points). See Extended Data Figure 2C for representative mass histograms with the wild-type human dynein$_{MOTOR}$ protein with and without LIS1 (from left to right, n = 6/6/5, 3/9/8, 5/5/6, 4/8/6, and 5/4/9 independent replicates).

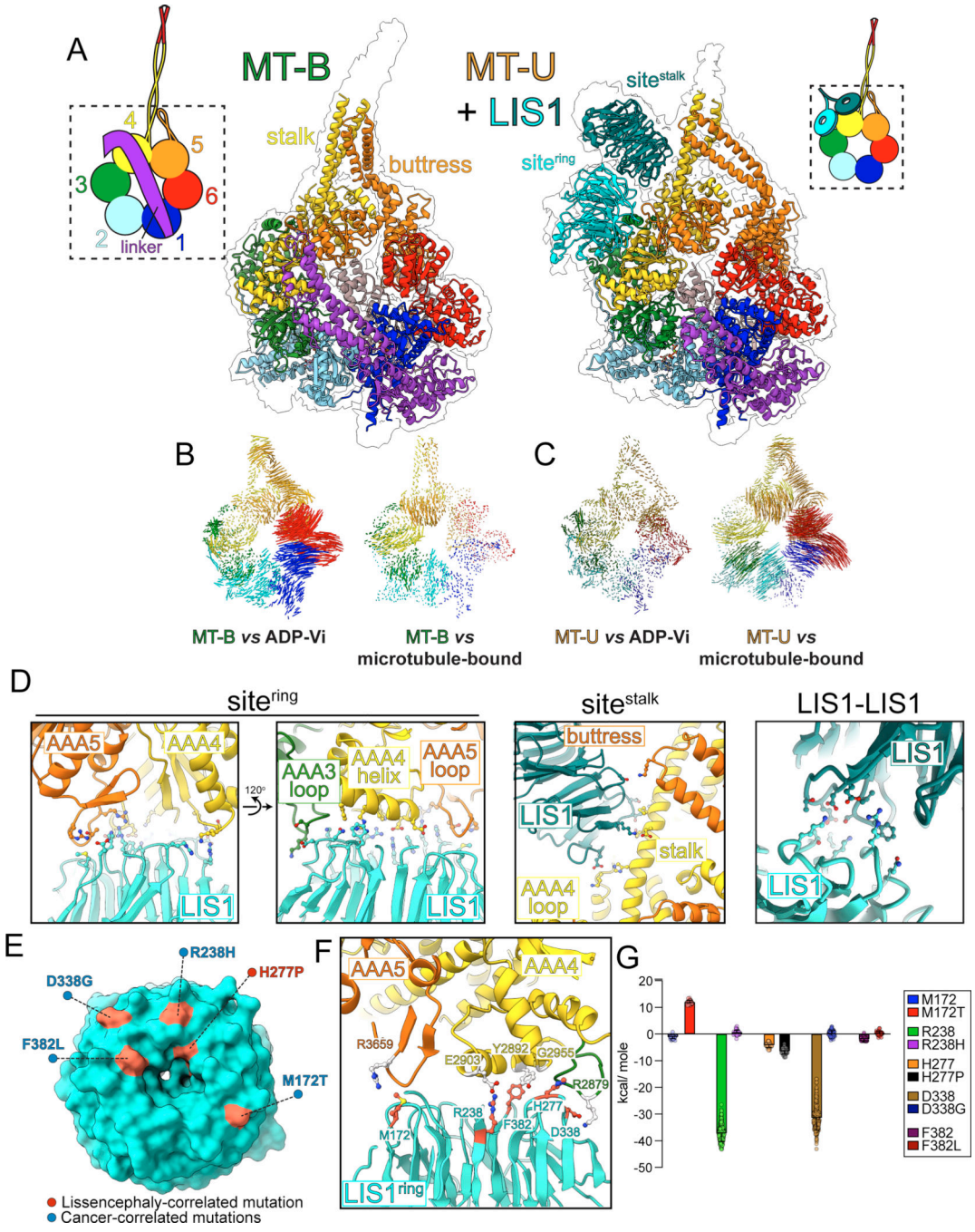

Figure 5. Cryo-EM structures of human dynein$_{MOTOR}^{MT-B}$ and a LIS1-bound dynein$_{MOTOR}^{MT-U}$.

(A) Molecular models of dynein$_{MOTOR}^{MT-B}$ (solved in the presence of ATP) and LIS1-bound dynein$_{MOTOR}^{MT-U}$ (solved in the presence of ATP and Vi) with corresponding density maps (indicated with outlines). Subdomains are color-coded as indicated by cartoon. (B and C) Vector maps depicting pairwise alpha carbon interatomic distances between dynein$_{MOTOR}^{MT-B}$ (B) or dynein$_{MOTOR}^{MT-U}$ (C) with either the human ADP-Vi-bound dynein-2 crystal structure (4RH7)[37], or the native microtubule-bound dynein-1 cryo-EM structure (7Z8G)[38]. Structures were globally aligned after removal of the linkers. The

length of the lines are proportional to the calculated interatomic distances. Note the strong similarities between dynein$_{MOTOR}^{MT\text{-}B}$ and the microtubule-bound dynein (but not with 4RH7), and that of dynein$_{MOTOR}^{MT\text{-}U}$ with the ADP-Vi-bound dynein (but not with 7Z8G). (D) Close-up views of the main contact points between LIS1 with site^{ring} and site^{stalk} (as indicated), and between the two LIS1s within the homodimer. Also see Video S2. Residues with atoms shown are those determined to mediate contacts (see Extended Data Figure 6B). (E) Surface view showing site^{ring}-bound LIS1 with disease-correlated residues highlighted. (F) Close-up view of contact points between disease-correlated residues on LIS1 and site^{ring}. (G) Plot (mean ± SD, along with all data points) depicting results of molecular dynamics simulations depicting energy of interaction between LIS1 and either wild-type or mutant dynein, as indicated (from left to right, sampling numbers = 40, 43, 256, 46, 41, 46, 243, 81, 84, and 46). See Extended Data Figure 6D for graphical depiction of MD simulation data.

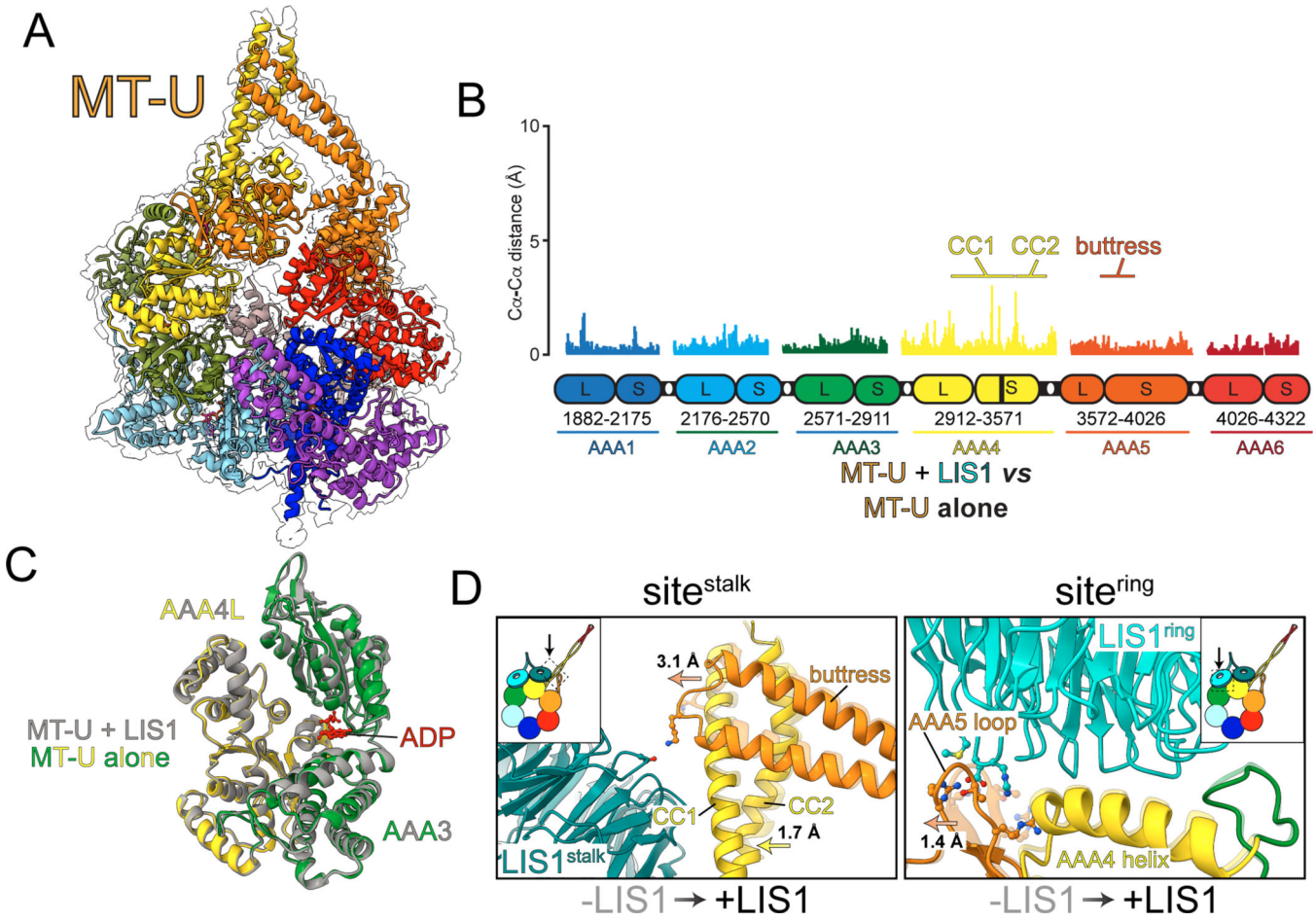

Figure 6. Cryo-EM structure of human dynein$_{MOTOR}^{MT-U}$ alone.

(A) Molecular model of dynein$_{MOTOR}^{MT-U}$ (solved in the presence of ATP and Vi) with corresponding density map (indicated with outline). Subdomains are color-coded as indicated by cartoon shown in Figure 5A. (B) Plot depicting pairwise alpha carbon interatomic distances between the dynein$_{MOTOR}^{MT-U}$ with and without LIS1. Note the high degree of similarity between the two structures, with minor exceptions in CC1 and CC2 (see text). (C) AAA3-AAA4L domains from dynein$_{MOTOR}^{MT-U}$ with (grey) and without LIS1 (green and yellow) overlaid to depict the high degree of structural similarity. (D) Close-up views illustrating the differences in dynein structure with and without LIS1 at the contact points between dynein and LIS1. The structure without LIS1 is depicted with reduced opacity compared to that with LIS1. Note the small shifts in the buttress tip toward site^{stalk}-bound LIS1, and of the AAA5 loop away from site^{ring}-bound LIS1.

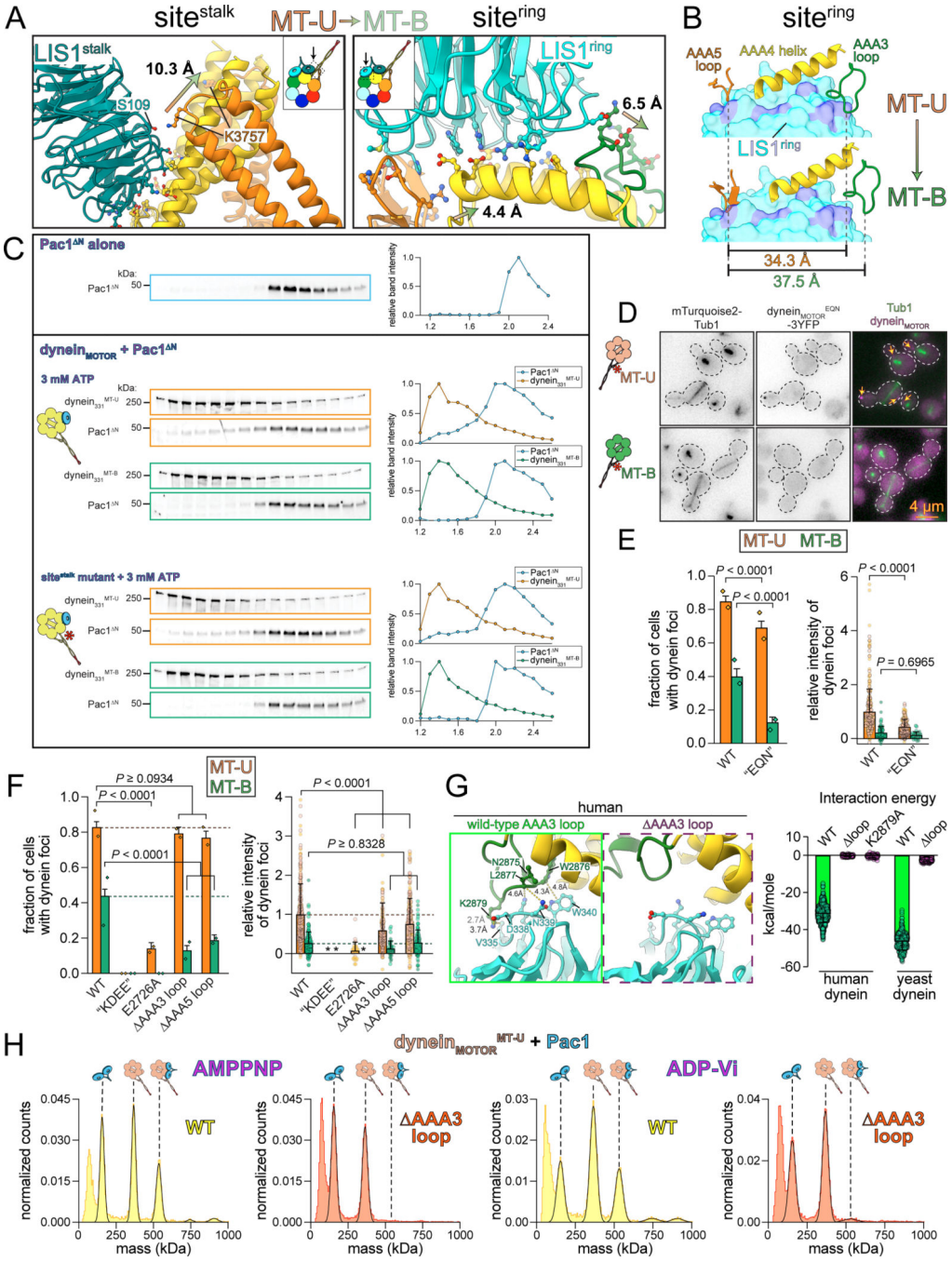

Figure 7. Changes at site^{ring} account for reduced LIS1/Pac1 binding affinity.

(A) Close-up views illustrating differences between dynein$_{MOTOR}^{MT-U}$ and dynein$_{MOTOR}^{MT-B}$ at site^{stalk} and site^{ring} (dynein$_{MOTOR}^{MT-B}$ is depicted with reduced opacity compared to dynein$_{MOTOR}^{MT-U}$). Arrows indicate notable differences. Residues with atoms shown are those determined to mediate contacts between dynein and LIS1. (B) Summary of major changes at site^{ring}. Purple residues on LIS1 are those that make contact with site^{ring}. (C) Analytical size exclusion chromatography analysis showing monomeric Pac1$^{\Delta N}$ alone, or mixed with indicated yeast dynein$_{MOTOR}$ prior to running on a Superdex

5/150. Plots depict band intensity profiles. Gels and analysis are representative of at least 3 independent replicates. (D) Representative images of cells expressing mTurquoise2-Tub1 and indicated dynein$_{MOTOR}$ with "EQN" mutations (arrows, plus end foci). (E and F) Plots (mean ± SD, along with all data points) depicting frequency and relative intensity of indicated dynein foci (for panel E: n = 300 foci from 246 $dyn1_{MOTOR}^{MT\text{-}U}$ cells; 95 foci from 222 $dyn1_{MOTOR}^{MT\text{-}B}$ cells; 232 foci from 290 $dyn1_{MOTOR}^{MT\text{-}U\ [EQN]}$ cells; 33 foci from 220 $dyn1_{MOTOR}^{MT\text{-}B\ [EQN]}$ cells; for panel F: n = 339 foci from 263 $dyn1_{MOTOR}^{MT\text{-}U}$ cells; 158 foci from 316 $dyn1_{MOTOR}^{MT\text{-}B}$ cells; 0 foci from 203 $dyn1_{MOTOR}^{MT\text{-}U[KDEE]}$ cells; 0 foci from 284 $dyn1_{MOTOR}^{MT\text{-}BU[KDEE]}$ cells; 31 foci from 212 $dyn1_{MOTOR}^{MT\text{-}U[E2726A]}$ cells; 0 foci from 284 $dyn1_{MOTOR}^{MT\text{-}B[E2726A]}$ cells; 229 foci from 251 $dyn1_{MOTOR}^{MT\text{-}U[\Delta AAA3\ loop]}$ cells; 41 foci from 284 $dyn1_{MOTOR}^{MT\text{-}B[\Delta AAA3\ loop]}$ cells; 312 foci from 238 $dyn1_{MOTOR}^{MT\text{-}U[\Delta AAA5\ loop]}$ cells; 92 foci from 319 $dyn1_{MOTOR}^{MT\text{-}B[\Delta AAA5\ loop]}$ cells; all from 2 biological replicates). (G) Plot (mean ± SD, along with all data points) depicting results of MD simulations depicting energy of interaction between wild-type or mutant human or yeast dynein with LIS1 or Pac1 (from left to right, sampling numbers = 1024, 163, 134, 335, 401). (H) Mass photometric analysis of indicated proteins in the indicated nucleotides. Histograms depict representative data of at least 3 independent replicates for each, all of which showed the same results. For panels E and F, two-tailed *P* values were calculated from Z scores for proportion data, or by comparing means using a Dunnett's test (for intensity values).

Table 1.

Cryo-EM Data Collection, Refinement, and Validation Statistics.

Description	MT-B Full Map (EMD-2899) (PDB 8FCY)	MT-U Full Map (EMDB-29003) (PDB 8FD6)	MT-U+2Lis1 Full Map (EMDB-29012) (8FDT)	MT-U+2Lis1 AAA3-AAA5+2lis Local Refined Map (EMDB-29014) (PDB 8FDU)
Data Collection and Processing				
Microscope	Glacios	Glacios	Titan Krios	
Voltage (kV)	200	200	300	
Camera	K2	K2	K3	
Magnification	36,000	36,000	105,000	
Pixel Size (Å)	1.149	1.149	0.825	
Total Electron Exposure (e-/A^2)	40	40	50	
Defocus Range (μm)	1.5–2.7	1.5–2.7	1.5–2.7	
Symmetry Imposed	C1	C1	C1	
Initial Particles	250 463	729 028	1 400 918	
Final Particles	44 752	201 707	53 572	
Refinement				
Initial models	5NUG	5NUG	5NUG, 7MGM, Alphafold	5NUG, 7MGM, Alphafold
Map pixel size	1.149	1.149	1.149	1.149
Map Resolution (FSC 0.143)	3.4	2.9	3.2	3.2
Map Resolution (3D FSC)	3.5	3.0	3.4	3.4
Map resolution range (Å)	3.1–10	2.8–10	3.0–10	3.0–10
Map sharpening B-factor (Å^2)	−56	−64	−44	−52
Model Composition				
Non-hydrogen atoms	23 157	22182	27103	13189
Protein residues	2866	2749	3370	1633
Ligands	ATP (1)/ADP (3)	ATP (1)/ADP (3) VO4 (1)/Mg^{2+} (1)	ATP (1)/ADP (3) VO4 (1)	ADP (2)
Model vs. Data				
FSC Map to Model (FSC 0.5)	3.7	3.2	3.7	3.6
Correlation coefficient (mask)	0.86	0.80	0.80	0.79
B factors (A ^{2})				
Protein	95.89	79.10	87.63	101.23
Nucleotide	77.44	59.87	56.36	76.23
R.m.s deviation				
Bond length (Å)	0.002	0.006	0.003	0.004

Description	MT-B Full Map (EMD-2899) (PDB 8FCY)	MT-U Full Map (EMDB-29003) (PDB 8FD6)	MT-U+2Lis1 Full Map (EMDB-29012) (8FDT)	MT-U+2Lis1 AAA3-AAA5+2lis Local Refined Map (EMDB-29014) (PDB 8FDU)
Bond angles (°)	0.549	0.671	0.607	0.680
Validation				
Molprobity score	1.74	1.76	1.80	1.87
Clashscore	7.86	9.20	10.91	12.64
Rotamer outliers (%)	0.08	0.00	0.00	0.00
Ramachandran plot				
Outliers (%)	0.04	0.00	0.06	0.00
Allowed (%)	4.45	3.95	3.58	3.75
Favored (%)	95.52	96.05	96.36	96.25
Rama-Z (whole)	0.50	0.43	0.69	−0.17